

GPU-Beschleunigung der Material Point Method

Masterarbeit

zur Erlangung des Grades Master of Science (M.Sc.)
im Studiengang Computervisualistik

vorgelegt von
Fabian Meyer

Erstgutachter: Prof. Dr.-Ing. Stefan Müller
(Institut für Computervisualistik, AG Computergraphik)

Zweitgutachter: Bastian Kray, M.Sc.
(Institut für Computervisualistik, AG Computergraphik)

Koblenz, im Januar 2019

Erklärung

Ich versichere, dass ich die vorliegende Arbeit selbständig verfasst und keine anderen als die angegebenen Quellen und Hilfsmittel benutzt habe.

Ja Nein

Mit der Einstellung der Arbeit in die Bibliothek bin ich einverstanden. ☐ ☐

.....
(Ort, Datum) (Unterschrift)

Zusammenfassung

Die Material Point Method hat sich in der Computergrafik für physikalische basierte Simulationen etabliert. Sie benutzt ein hybrides Modell aus Lagrange-Partikeln und Euler-Gitter. Während Partikel als konsistenter Speicher fungieren, erlaubt das Gitter anfallende partielle Differentialgleichungen effizient zu lösen.

Die Material Point Method unterliegt hohen Berechnungszeiten, die die Methode nur für Hero Shots rentabel macht. Sie ist jedoch hoch-parallelisierbar. Diese Arbeit zeigt, wie die Methode mit GPGPU-Techniken beschleunigt werden kann.

Der Datenaustausch von Partikel und Gitter wird über interpolierende Transfers erreicht. Pro physikalischen Zeitschritt werden diese mehrmals ausgeführt. Vorverarbeitungsschritte können unternommen werden, um diese Transfers performanter zu machen.

Countingsort für jede Partikel-Variable erhöht Coalescing und L2-Cache Hitraten. Binning teilt das Gitter in Blöcke auf, die Shared-Memory Implementationen ermöglichen. Die Größen der Bins sind für keine Operation beschränkt. Weiterhin werden nur Blöcke ausgeführt, die Informationen erhalten.

Abstract

The material point method is allowing for physically based simulations. It has found its way into computer graphics and since then rapidly expanded. The material point method's hybrid use of Lagrangian particles as a persistent storage and a background uniform Eulerian grid enables solving of various partial differential equations with ease.

The material point method suffers from high execution times and is thus only viable for hero shots. The method is however highly parallelizable. Thus, this thesis proposes how to accelerate the material point method using GPGPU techniques.

Core of the material point method are grid and particles transfers that interpolate between the two structures. These transfers are executed multiple times per physical time step. Preprocessing steps might be taken if their computing time is outweighed.

Deep sorting with counting sort increases coalescing and L2 cache hit rates. Binning allows to divide the grid into blocks for shared memory filtering techniques. All operations do not rely on fixed bin size. As another preprocessing step, only grid blocks are executed which have particles in them.

Contents

1	Introduction	1
2	Related Work	3
3	Notation	7
4	Basics	9
4.1	Reference and current configuration	9
4.2	Polar and singular value decomposition	11
4.3	Constitutive models	13
4.3.1	Linear elasticity	13
4.3.2	Corotated hyperelasticity	15
4.3.3	Fixed corotated hyperelasticity	16
4.4	Governing equations	16
4.4.1	Conservation of mass	16
4.4.2	Conservation of momentum	17
4.4.3	Weak formulation	19
4.5	Material point method	21
4.5.1	Interpolation weights	21
4.5.2	Mass transfer	22
4.5.3	APIC-transfers	22
4.5.4	CFL condition	24
4.6	Discretization	25
4.6.1	Discretize time	25
4.6.2	Discretize space	25
4.6.3	Deformation gradient evolution	27
4.6.4	Grid nodal forces	28
4.6.5	Symplectic midpoint scheme	28
4.6.6	Newton's Method	29
4.7	General-purpose computing on graphics processing units	32
4.7.1	GPGPU Optimization opportunities	32
4.7.2	GPU Metrics	34
5	Implementation	36
5.1	GPU memory layout	36
5.2	Parallel Reduction & Scan	38
5.3	Counting sort & stream compaction	41
5.4	MPM operations	42
5.4.1	Grid-to-particle transfers	44
5.4.2	Particle-to-grid-transfers	46
5.4.3	Active blocks & maximum block count:	49

6	Evaluation	51
6.1	Verifying Results	51
6.2	Performance	52
7	Conclusion & Future Work	62
	Appendices	64
A	D_p for Cubic Splines	64
B	Block Scan	65
C	Shared memory accesses on MPM-Transfers	68

1 Introduction

General purpose computation on graphics processing unit(GPGPU) has elevated graphics processing units(GPUs) to any computational field utilizing massively parallelizable algorithms. As such is the nature of discretizations in physics.

The higher parallelization acceleration of GPUs is a blessing for those applications that can profit from it. In unison with efficient algorithms they still have much potential to offer. Conversely, algorithms which are not parallelizable perform much worse and should be avoided. Dividing up these tasks between CPU and GPU is not recommendable. Transferring data over the PCI-Bus between the two is slow for big amounts of data and requires synchronization. Tasks in such a pipeline should thus stay on the GPU although they might perform worse.

Programming for the GPU is another hurdle. GPU code is reliant on the generation and hardware vendor of the GPU to use relevant extensions. Backwards compatibility therefore is mostly ignored and written towards a certain GPU generation. This is amplified due to the GPU code often being reliant on architecture limits for maximum performance. The major languages to target the GPU are CUDA, OpenCL, Direct 3D, OpenGL, and Vulkan. They build on top of a C/C++-language subset.

Whereas CUDA offers the most libraries and optimized code, it is only available on NVIDIA GPUs. OpenCL's development on NVIDIA GPUs is dragging far behind the standard. Its merge into the Vulkan roadmap could be an incentive to support a more in-depth language universally [Mic17]. Direct3D is only available on Windows. Vulkan is the successor of OpenGL and removes work from the driver to the developer. Main benefit over OpenGL is less CPU usage which helps little for the almost full GPU implementation here. This implementation opts for OpenGL as Vulkan is still relatively new. Everything presented could be implemented in one of the other languages as well.

The simulation of the dynamics of materials is still extremely challenging in different applications and fields. Multiphysics interactions between materials are not realized on a big scale and often are not possible or feasible. The material point method(MPM) has already reliably tackled many different models, materials, and even interaction between materials.

Pure Eulerian methods like the finite element method(FEM) have been in use for long in engineering tasks but face problems handling topology changes with numerical stability. Pure Lagrangian methods form the end other of the spectrum. Prominent are smoothed-particle hydrodynamics(SPH) that are restricted to (viscous) fluids and are of empirical nature. Particle in cell(PIC) techniques like the material point method are hybrid Lagrangian/Eulerian methods. They try to benefit from the nature of both. Advection on particles is trivial. Thus the material point method utilizes Lagrangian particles as a consistent storage of dynamic properties. The governing equations of the physical problem can be discretized easily to and solved on a uniform Eulerian grid. The grid is unmoving and does not store any information between physical time steps.

Transfers between the Lagrangian and Eulerian are of need to bring the two together. These transfers are the focus of particle in cell techniques. These transfers are realized due to interpolation. Thus they create (estimable) numerical error and lead to dissipation. Moreover grid nodes are mostly outnumbered by particles leading to more numerical error as modes of the single particles are not realized by the grid.

The p particles to one node relationship of a particle-to-grid(P2G)-transfer or inversely one node to p particles of a grid-to-particle(G2P)-transfer is the main problem when realizing these operations on the GPU. When faced with the static architecture of the GPU, this will inevitably lead to branch divergence of threads within a subgroup as some nodes are assigned more particles than others.

Chapter 2 looks at the relevant literature of PIC-Methods specifically on the GPU as well as material point method extensions. In chapter 3 notations which will be used throughout the thesis are laid out. The basics of chapter 4 cover the derivation of an elastic material in the MPM to get an understanding of the prominent operations. Furthermore GPU intrinsics, metrics and optimization opportunities are discussed. Chapter 5 tends to the implementation. The evaluation of the implementation follows up in chapter 6. As a conclusion chapter 7 gives a summarizing overview and tends to future work.

2 Related Work

Particle in cell techniques were developed initially for hydrodynamics [EHB57]. They are also widely used in plasma simulations to solve Maxwell's equations [Pay12]. Their key steps are identical to the MPM:

1. Transfer particle data to a grid.
2. Solve the governing partial differential equations on the grid to move forward in time.
3. Transfer grid data back to particles.

In general the grid is regarded as a scratch-pad since its only a temporary storage for the means of computing item 2. I.e. the grid could be deleted each physical times step. Based on PIC to reduce dampening and momentum conservation Fluid-Implicit-Particle (FLIP) was developed for fluid simulations and is still widely in use for large simulations. Their counterpart being the empirical smoothed-particle hydrodynamics [GM77].

As a further development the Affine-particle in cell (APIC) technique was introduced as an improvement to PIC and FLIP solvers. Due to the definition of a local affine velocity field around each particle (instead of a single vector) APIC conserves angular momentum, reduces damping and improves stability over PIC and FLIP, more in chapter 4.5.3. [JST17] [Jia+15]

A step further goes PolyPIC giving the velocity field even more freedom by adding polynomial velocity modes of increasing order to the description. [Fu+17]

The **material point method** is a further development to the PIC methods. Both use analysis and numerics to be derived without the need for empirical assumptions. Originally it was developed by [SZS95] with a focus on the dynamics of solids. [Sto+13] brought the method into computer graphics for their animation film *Frozen*. In rapid succession a variety materials and effects got modeled by the MPM. Since MPM is based on discretizing governing equations and using constitutive models covered by the different literature, its fast rate of expenditure is not a surprise.

The simulation of (hyper-)elastic materials can be done with a number of different strain measures utilizing fixed Linear strain (chapter 4.3.2), Green-Lagrangian strain tensor (chapter 4.2), or logarithmic Hencky-strain ([Guo+18]) for the different requirements of small to large strains. Inserting these into the different energy density $\Psi(\epsilon)$ models can already result in a constitutive model. Plasticity in general requires extra modeling in terms of a flow rule, yield-condition, and a hardening rule which are not discussed here [Öch14]. To give a short impression of the developments in computer graphics:

[Sto+14] model phase transition (melting) to a liquid with using the fixed corotational hyperelasticity model (chapter 4.3.2) in combination with a discretization of the heat equation. [Ram+15] use an Olroyd-B model with Cauchy-Green

strain to handle elasticity and plasticity for viscoelastic fluids, foams, and sponges. [Klá+16] uses Hencky-strain in combination with a St. Venant-Kirchhoff model and Drucker-Prager elastoplasticity to model sand. [Tam+17] combine particles of different species (sand and water) by one grid for each species and relating them with a heuristic momentum exchange. [Guo+18] simulates thin shells (cloths, cups etc.) with a Kirchhoff-Love model using Hencky-strains.

There exist several implementations utilizing the **GPU for particle in cell** techniques, which the material point method is a part of:

Particle sorting: [Pay12] studies different particle list sorting methods. Methods like 'Message Passing Sort' [Kon+11] [DS11], 'In Place Particle-QuickSort' [SDG08] and 'Linked List Ordering' [Bur+10] try to utilize the partial sorting and only update particles that need to be moved within the list. These methods often rely on the assumption that only a small number of particles change their grid node, where in contrast MPM can be quite dynamic. Those that do move, move at most to one neighboring grid-node or stay in the same node due to the CFL condition, chapter 4.5.4. These methods often use fixed bin-sizes which can be quite memory intensive and add additional memory management. Fixed size binning makes the methods mentioned before easier to implement which don't necessarily map well to the GPU due to their high complexity and uncoalesced accesses. As a result [Pay12] come to the conclusion to fall back to the CUDA library `thrust`, although they do note that the aforementioned methods can perform faster for particles that move only a limited amount of grid nodes. `thrust` provides the radix sort method `thrust::sort_by_key()`, where one sorts by grid index as key.

In general deep or index sorts can be done. A deep sort reorders every variable of a particle. An index sort gives back an index with an offset to access the particle variable.

[Hoe14] compare radix to counting sort utilizing a uniform grid and use the latter for SPH-fluids.

This implementation compares index and deep counting sort and uses the latter. Although possible, this counting sort stays away from the limited movement implied by the Courant-Friedrichs-Lewy(CFL) condition. Fixed size bins are an assumption this implementation also does not want to impose on the method.

Particle-to-grid-transfers are generally done in two manners [SDG08]:

1. **Particle push:** X particles in a local neighborhood of a grid point push their attributes onto it. Since this relationship results in a race condition `atomicAdd(float f)s` or explicit synchronization is necessary, e.g. `atomic`: [Pay12], synchronized: [Ros13].
2. **Particle pull:** A grid point pulls the particles in its local neighborhood from a sorted particle list. This has the benefit of no race conditions being present.

A **grid-to-particle-transfer** is in general easier since a particle already knows, due to its position, the grid points in its local neighborhood. The grid points in a

uniform grid are 'sorted' by nature. This implementation tests one particle pull and two particle push methods.

Generally these methods are augmented by splitting the grid in 2D/3D blocks making use of the shared memory structure of the GPU [Pay12] [Hön+] [Klá+17], often called domain decomposition. Shared memory is however limited per GPU (GTX 970, 48KB per block [NVId]). The grid nodes reached by the support of the interpolation function on each side also have to be loaded into memory, typically called the halo of a block. Since the number of particles per grid point in the MPM is generally between 4-10, only very limited block sizes are available for pull methods that greedily load all particles [Sto+13].

Stencil computations and filtering techniques underlie a very similar process to MPM-transfers. Although these techniques employ a one-to-one grid relationship, since no particles are involved, it is worth taking a look at them. An interesting prospect for filtering techniques on the GPU is given by NVIDIA's new shuffle operations. Shuffle allows to 'share' register memory between threads of a warp [Wes15]. They are however not supported on other architecture, yet.

Widely used is a 2.5D blocking: A domain (of the domain decomposition) is split into 2D-planes along one axis. Data reuse of shared memory is maximized by a cyclic-queue strategy: Start a thread for each grid node in the first plane and load the halo along the axis into shared memory. Then each thread iterates along the axis over the 2D-planes synchronously, discarding the oldest plane in memory while loading the next plane (along the axis) into shared memory. Thus there are no z-dimension halos. This however requires all particles in the halo to be present in the limited shared memory. As mentioned, this implementation wants to stay away from assumptions limiting particles similar to fixed bin sizes. [BP10] [Wil+07] [KD13]

In particle push methods partial sums are also computed on the halo. Two different techniques exist to get the data between blocks coherent again:

1. Atomically add up the values of the halo. This results in two atomic adds on a side node, four on an edge node, and eight on a corner node; If the block extend is bigger than half the halo extend, otherwise more.
2. Every halo of every block corresponds to actual global memory. After a transfer, do add steps along each of the three axes. This is infeasible for large supports due to the added memory requirements. [Cra+11]

Particle activation: If the particle's velocity is under a user-defined threshold, it becomes deactivated. It does not get recognized by any particle-to-grid-transfer, nor the grid solve(, nor any grid-to-particle-transfer not affected by the velocity transfer). They may of course be reactivated if the velocity in the neighborhood exceeds that threshold again or they collide. [Klá+17]

Dividing the particles up can be realized with stream compaction algorithms discussed in chapter 5.

Particle resampling: A method that could alleviate pressure off fixed bin sizes and make shared-memory restrictions less of a factor is particle resampling. Their intention mostly is to fill numerical gaps in the material at large deformations where the material is not supposed to break yet. Split and merge methods can directly control how many particles in a cell are allowed and accordingly increase or reduce them.

A simple *Split* method divides one particle into eight with a distance of half the diagonal length of a grid cell from the original particle. The eight particles span a cube that can be randomly rotated if desired. Mass and volume get equally distributed; Velocity and deformation gradient get copied. Refer to chapter 4.5 or for conservation of mass and momentum in MPM. [Gao+17]

A *Merge* method looks for the closest neighbors and creates the new merged particle at the geometric center. Mass and volume are accumulated. Velocity is computed from a mass-weighted average of the participating particles. The deformation gradient is accordingly to chapter 4.2 decomposed into $\mathbf{F} = \mathbf{U}\mathbf{\Sigma}\mathbf{V}^T$. The quaternion average of \mathbf{U} s and \mathbf{V} s of the particles lead to an average rotation $\overline{\mathbf{U}}$ and $\overline{\mathbf{V}}$, respectively. The principal strains within $\mathbf{\Sigma}$ are just averaged component-wise to $\overline{\mathbf{\Sigma}}$. One can compose them in the same fashion leading to an average deformation gradient with $\overline{\mathbf{F}} = \overline{\mathbf{U}}\overline{\mathbf{\Sigma}}\overline{\mathbf{V}}^T$. [Gao+17]

Unconditionally keeping particles on a fixed size is not desirable due to fracture requiring that gaps will be created. [Gao+17] produce a signed distance field to identify interior points. Surface points also should not merge or split due to visual artifacts. Furthermore, the signed distance field can be used to adapt the grid size depending on the distance to the surface. This allows for coarser levels with increasing distance from the surface.

3 Notation

Multi-component types are generally printed in bold letters \mathbf{A} , \mathbf{a} . Vectors furthermore use lower-case letters \mathbf{v} with the exception of angular momentum \mathbf{L} ; Matrices use upper-case letters \mathbf{M} . A variable in the Lagrangian form has a left subscript 0: ${}_0\mathbf{x}$. The Eulerian description has a left subscript t : ${}_t\mathbf{x}$. Occasionally, notation may be omitted where it is apparent from context.

Beginning from chapter 4.5 variables defined on a particle will have right subscript p (e.g. \mathbf{x}_p). Grid cells will be assigned a right subscript i or additionally j denoting the grid index (e.g. \mathbf{x}_i). This is not to be confused with the following Einstein-notation. Therefore, beginning with chapter 4.5 Einstein-notation for components will use greek letters (α, β) . Occasionally summation over grid index i and particles p may be implied. A variable of the n -th time step with associated time $t^n = \sum_{i=1}^{n-1} \Delta t^i$ will have a right superscript: \mathbf{x}^n .

Used throughout this thesis is at instances the **Einstein-notation** when using tensors and vectors.

Repeated indices, that are also defined on the variable, imply component-wise operations. Let \mathbf{a} and \mathbf{b} be vectors of dimension n and $\mathbf{A}, \mathbf{B}, \mathbf{D}$ $m \times n$ tensors. $a_i b_j$ is multiplying component i with component j of vectors \mathbf{a} and \mathbf{b} . Vector and tensor/matrix addition thus become:

$$c_i = a_i + b_i \quad \text{and} \quad D_{ij} = A_{ij} + B_{ij}. \quad (1)$$

A transpose operator swaps the indices:

$$D_{ij}^T = D_{ji}. \quad (2)$$

Repeated indices, that are not otherwise defined, however imply summation on that index. The vector dot product becomes:

$$a_i b_i \equiv \sum_{i=1}^n a_i b_i. \quad (3)$$

Following this notation the Frobenius inner product between two second-order tensors is (also called Frobenius scalar product):

$$\mathbf{A} : \mathbf{B} \equiv A_{ij} B_{ij} \equiv \sum_{i=1}^n \sum_{j=1}^m A_{ij} B_{ij}. \quad (4)$$

The Frobenius inner product between a $r \times s \times m \times n$ fourth-order tensor \mathbf{C} and second-order tensor creates a second order tensor combining the ideas of 1 and 4:

$$\mathbf{A} = A_{ij} = \mathbf{C} : \mathbf{B} = C_{ijkl} B_{kl} = \sum_{k=1}^m \sum_{l=1}^n C_{ijkl} B_{kl}. \quad (5)$$

Matrix-Vector and Matrix-Matrix multiplication can be expressed this way as:

$$b_i = A_{ij}a_j \quad D_{ij} = A_{ik}B_{kj}. \quad (6)$$

The definition of the Kronecker Delta is as follows:

$$\delta_{ij} = \begin{cases} 1 & \text{if } i = j \\ 0 & \text{if } i \neq j \end{cases}. \quad (7)$$

The Kronecker Delta as an operator is most efficiently described as a substitution:

$$a_i \delta_{ij} = a_j. \quad (8)$$

I.e. this component is only evaluated if $i = j$. The Kronecker Delta comes up in differentiating a variable by itself with same or different index:

$$\frac{\partial x_0}{\partial x_1} = 0, \frac{\partial x_0}{\partial x_0} = 1 \Rightarrow \frac{\partial x_i}{\partial x_j} = \delta_{ij}. \quad (9)$$

The alternating tensor or Levi-Civita symbol

$$\varepsilon_{ijk} = \begin{cases} +1 & \text{if } (i, j, k) \text{ is } (1, 2, 3), (2, 3, 1), \text{ or } (3, 1, 2) \\ -1 & \text{if } (i, j, k) \text{ is } (3, 2, 1), (1, 3, 2), \text{ or } (2, 1, 3) \\ 0 & \text{if } i = j, \text{ or } j = k, \text{ or } k = i \end{cases} \quad (10)$$

is used to express cross-products $\mathbf{c} = \mathbf{a} \times \mathbf{b}$:

$$c_i = \varepsilon_{ijk}a_jb_k \left(= \sum_{j=1}^n \sum_{k=1}^n \varepsilon_{ijk}a_jb_k \right). \quad (11)$$

A useful relation to the Kronecker-Delta is:

$$\varepsilon_{ijk}\varepsilon_{imn} = \delta_{jm}\delta_{kn} - \delta_{jn}\delta_{km}. \quad (12)$$

[McG]

4 Basics

The first chapters will derive the material point method and necessary extensions for an elastic model. An elastic model is an interesting case displaying much of the needed computations for a typical model. The last chapter 4.7 tends to the GPGPU side.

4.1 Reference and current configuration

Particles (or material points) in continuum mechanics are not what classically might be thought of as a particle. Rather, the continuum assumption holds: Each particle represents a continuous piece of material s.t. a microscopic view does not need to be adopted. A particular body is composed of a set of particles and can adapt different configurations due to changes in shape. These changes are caused by external or internal effects (forces etc.) on it and deform the body over time. [Abe12] [Jia+16]

When modelling solids, changes of quantities from an initial reference configuration ${}_0\mathbf{x}$ to another current configuration ${}_t\mathbf{x}$ need to be measured. In the material point method the reference configuration ${}_0\mathbf{x}$ is just the initial configuration of the body (at time $t = 0$). This is similar to the total Lagrangian formulation in finite element methods [Bat06].

Let $\Omega^0, \Omega^t \subset \mathbb{R}^3$ be the set of (material) points in the reference and current configuration respectively. Then one may define a function or mapping ${}_0^t\phi(\cdot, t) : \Omega^0 \rightarrow \Omega^t$ which relates the reference configuration to the current configuration. Let for simplicity ${}_0\mathbf{x}$ and ${}_t\mathbf{x}$ describe the position of the particle in their respective configurations. Then this mapping becomes the deformation of the body from the reference configuration ${}_0\mathbf{x}$:

$${}_t\mathbf{x} = {}_0^t\phi({}_0\mathbf{x}, t) \quad (13)$$

If for instance the body consisting of each material point ${}_t\mathbf{x}$ moves with velocity \mathbf{v} and rotation $\mathbf{R}(t)$, this mapping is defined as:

$${}_t\mathbf{x} = {}_0^t\phi({}_0\mathbf{x}, t) = \mathbf{R}(t){}_0\mathbf{x} + \mathbf{v}t \quad (14)$$

The velocity of a material point in the reference configuration can be defined using this mapping

$${}_0\mathbf{v}({}_0\mathbf{x}, t) = \frac{\partial({}_0^t\phi)}{\partial t}({}_0\mathbf{x}, t), \quad (15)$$

and similarly the acceleration is defined

$${}_0\mathbf{a}({}_0\mathbf{x}, t) = \frac{\partial^2({}_0^t\phi)}{\partial t^2}({}_0\mathbf{x}, t) = \frac{\partial{}_0\mathbf{v}}{\partial t}({}_0\mathbf{x}, t). \quad (16)$$

It is helpful to abstract away from the reference configuration and think of it as being defined in a different fixed material space. Physically this has the impact of moving with the particle in world space. Commonly known as the Lagrangian

form. It is often easier in continuum mechanics to start with a Lagrangian description and switch to a Eulerian one if needed. The Eulerian description is static: Variables of particles moving by are measured while staying in a fixed position.

These descriptions are different but they will yield the same measurements when related correctly. I.e. both configurations refer variables defined on them to the deformed state but the position, where the 'lookup' of that value happens, is different. In the reference configuration lookup is done at the initial position of the particle. In the current configuration lookup happens at the particle's world position. These relations for some particle quantity f are called the (Lagrangian) pull back

$${}_0f({}_0\mathbf{x}, t) = {}_tf({}_0^t\phi({}_0\mathbf{x}, t), t) \quad (17)$$

and the (Eulerian) push forward

$${}_tf({}_t\mathbf{x}, t) = {}_0f({}_0^t\phi^{-1}({}_t\mathbf{x}, t), t) = {}_0f({}_t^0\phi({}_t\mathbf{x}, t), t) \quad (18)$$

with definitions over their respective spaces ${}_tf(\cdot, t) : \Omega^t \rightarrow \mathbb{R}$, ${}_0f(\cdot, t) : \Omega^0 \rightarrow \mathbb{R}$. To enable the operator ${}_0^t\phi$ to be homeomorphic, s.t. an inverse ${}_0^t\phi^{-1} = {}_t^0\phi$ is defined, it is assumed that no two particles will ever occupy the same space at the same time.

The difficulty in the eulerian formulation becomes apparent when differentiating (due to the chain rule):

$$\frac{\partial}{\partial t}{}_0f_i({}_0\mathbf{x}, t) = \frac{\partial {}_tf_i}{\partial t}({}_0^t\phi({}_0\mathbf{x}, t), t) + \frac{\partial {}_tf_i}{\partial x_j}({}_0^t\phi({}_0\mathbf{x}, t), t) \frac{\partial {}_0^t\phi_j}{\partial t}({}_0\mathbf{x}, t). \quad (19)$$

Combining this with equation 15 and applying the push forward 18 to cancel out mappings leads to the definition referred to as the material derivative in the current configuration:

$$\frac{D}{Dt}f({}_t\mathbf{x}, t) = \frac{\partial f}{\partial t}({}_t\mathbf{x}, t) + \frac{\partial f}{\partial x_j}({}_t\mathbf{x}, t)v_j({}_t\mathbf{x}, t). \quad (20)$$

The Jacobian of the deformation map ϕ is the deformation gradient \mathbf{F} and is one of the key components to measure strain for material models:

$${}_0^tF_{ij}({}_0\mathbf{x}, t) = \frac{\partial {}_0^t\phi_i}{\partial {}_0x_j}({}_0\mathbf{x}, t) = \frac{\partial {}_tx_i}{\partial {}_0x_j}({}_0\mathbf{x}, t). \quad (21)$$

Topology specifies a neighborhood using the open ball concept ${}_0, {}_tB_\epsilon(\mathbf{x}) = \{\mathbf{y} \in \Omega^{0,t} | d(\mathbf{x}, \mathbf{y}) < \epsilon\}$ given a distance measure d . ${}_0B_\epsilon$ becomes the pre-image of ${}_tB_\epsilon$ under ${}_0^t\phi$. Intuitively the deformation gradient measures the local deformation of all particles in a small neighborhood ${}_0B_\epsilon$ to ${}_tB_\epsilon$. This allows to describe infinitesimal changes in position from the reference to the current configuration

$$d_tx_i = {}_0^tF_{ij}d_0x_j. \quad (22)$$

With this quantity in place volume and area changes are calculable. In a typical analytical fashion a coordinate system change ${}_0x \rightarrow {}_tx$ for a quantity ${}_0g$ is done using the determinant of the Jacobian matrix. The determinant is given a separate name ${}_0^tJ = \det({}_0^t\mathbf{F})$. The push forward of ${}_0g : \Omega^0 \rightarrow \mathbb{R}^d$ thus becomes ${}_tg : \Omega^t \rightarrow \mathbb{R}^d$:

$$\int_{{}_tB} {}_tg({}_tx, t) d{}_tx = \int_{{}_0B} {}_0g({}_0x, t) {}_0^tJ d{}_0x. \quad (23)$$

This can also be achieved by the cross product. A cube spanned by vectors ${}_0\mathbf{x}_i$ ($i = 1, 2, 3$) becomes a parallelepiped in the deformed configuration $d{}_tV = |{}_0^t\mathbf{F}d{}_0\mathbf{x}_0 \cdot ({}_0^t\mathbf{F}d{}_0\mathbf{x}_1 \times {}_0^t\mathbf{F}d{}_0\mathbf{x}_2)|d{}_0V$:

$$d{}_tV = {}_0^tJ d{}_0V. \quad (24)$$

The area change is given by Nanson's Formula. $d\mathbf{A}$ is a vector pointing in the direction of the normal of the area and $d{}_t\mathbf{l} = {}_0^t\mathbf{F}d{}_0\mathbf{l}$ an arbitrary line element:

$$\begin{aligned} d{}_0V &= d{}_0\mathbf{A} \cdot d{}_0\mathbf{l}, & d{}_tV &= d{}_t\mathbf{A} \cdot d{}_t\mathbf{l} \\ &\xrightarrow{22,24} {}_0^tJ d{}_0\mathbf{A} \cdot d{}_0\mathbf{l} &= d{}_t\mathbf{A} \cdot ({}_0^t\mathbf{F}d{}_0\mathbf{l}) \\ \Rightarrow d{}_t\mathbf{A} &= {}_0^t\mathbf{F}^{-T} {}_0^tJ d{}_0\mathbf{A} &= {}_0^t\mathbf{F}^T {}_0^tJ d{}_0\mathbf{A}. \end{aligned} \quad (25)$$

A surface integral may then be transformed to reference configuration by

$$\int_{\partial_0 B} \mathbf{h}({}_tx, t) \cdot d\mathbf{A}({}_tx) = \int_{\partial_t B} \mathbf{h}({}_0x, t) \cdot \mathbf{F}^{-T} J d\mathbf{A}({}_0x) \quad (26)$$

where ${}_0\mathbf{h} = \mathbf{h}({}_0x, \cdot)$ is the pull back of ${}_t\mathbf{h} = \mathbf{h}({}_tx, \cdot)$. $d{}_0\mathbf{A}$, $d{}_t\mathbf{A}$ point in the direction of the surface normal of $\partial_0 B({}_0x)$, $\partial_t B({}_tx)$, respectively. [Abe12] [Jia+16]

4.2 Polar and singular value decomposition

The target is to define strain measures in terms of the deformation gradient: $\epsilon(\mathbf{F})$. In equation 14 a rigid body movement was introduced. Let $b_i(t) = v_i t$ be more generally some translation. A problem arises when calculating the deformation gradient of this equation.

$${}_0^tF_{ij} = \frac{\partial {}_tx_i}{\partial {}_0x_j} = \frac{\partial (R_{ik}(t){}_0x_k + b_i(t))}{\partial {}_0x_j} = R_{ik}(t)\delta_{kj} = R_{ij}(t). \quad (27)$$

As can be seen, the deformation gradient contains a rigid rotation. For strain measures this is not beneficial as an assumption of the stiffness tensor requires no net-rotation (more in chapter 4.3.1). I.e. the deformation gradient has two components a constant rotation and the actual distortion or strain. There are two ways to deal with this:

1. Use a strain measure that cancels out the rotation. An example for this would be the Green-Lagrangian strain tensor with quadratic components:

$$E_{ij} = \frac{1}{2} (F_{ki}F_{kj} - \delta_{ij}). \quad (28)$$

2. Polar decompose the deformation gradient in its rotational \mathbf{R} and (symmetric positive definite) distortional \mathbf{S} parts $\mathbf{F} = \mathbf{R}\mathbf{S}$.

That equation 28 cancels out the rotational part can be shown by item 2:

$$\begin{aligned}\frac{1}{2}(F_{ki}F_{kj} - \delta_{ij}) &= \frac{1}{2}(S_{mi}R_{km}R_{kn}S_{nj} - \delta_{ij}) \\ &= \frac{1}{2}(S_{mi}\delta_{mn}S_{nj} - \delta_{ij}) = \frac{1}{2}(S_{im}S_{mj} - \delta_{ij}) \\ &= \frac{1}{2}(\mathbf{S}^2 - \mathbf{I}).\end{aligned}$$

Regarding item 2: Assuming a singular value decomposition of

$$\mathbf{F} = \mathbf{U}\mathbf{\Sigma}\mathbf{V}^T \quad (29)$$

is already computed where \mathbf{U}, \mathbf{V} are orthogonal matrices and $\mathbf{\Sigma}$ is a diagonal matrix containing the singular values $\sigma_1 \geq \sigma_2 \geq \dots \geq \sigma_r$ of \mathbf{F} . $(r - n)$ forms the dimension of the null space. The polar decomposition is computable as:

$$\mathbf{R} = \mathbf{V}\mathbf{W}^T, \quad \mathbf{S} = \mathbf{W}\mathbf{\Sigma}\mathbf{W}^T. \quad (30)$$

Since singular values are positive, it is straightforward to see that the properties for \mathbf{R} and \mathbf{S} hold. The components of the singular value decomposition are important to gain an intuition for its usefulness: The columns of \mathbf{U} and \mathbf{V} span bases for the row and column spaces of \mathbf{F} using the left and right singular vectors $\mathbf{u}_i, \mathbf{v}_i$, respectively [MIT]. For illustrating purposes imagine the manipulation of \mathbf{v}_1 due to $\mathbf{U}\mathbf{\Sigma}\mathbf{V}^T$:

1. Transform from the right singular vector space to standard basis space: $\mathbf{V}^T \mathbf{v}_1 = \mathbf{e}_1$.
2. Scale by singular values to transform to principal stretch space: $\mathbf{\Sigma} \mathbf{e}_1 = \sigma_1 \mathbf{e}_1$.
3. Transform to left singular vector space: $\mathbf{U} \sigma_1 \mathbf{e}_1 = \sigma_1 \mathbf{u}_1$.

For a positive definite matrix the singular value decomposition becomes even easier as $\mathbf{U} = \mathbf{V}$. Item 3 then effectively just becomes a transform 'back'.

In the following a summary of the 3×3 singular value decomposition as in [McA+11a] is given. The proposed singular value decomposition is also called the 'Polar SVD' and follows a specific convention.

1. \mathbf{U}, \mathbf{V} are reflection-free corresponding to true rotation matrices, i.e. both $\det(\mathbf{U}), \det(\mathbf{V}) = 1$ hold.
2. If $\det(\mathbf{F}) = -1$ the negative sign needs to move on to $\mathbf{\Sigma}$ as a result of item 1. The lowest singular value in magnitude will get a negative sign attached.

This convention does not change the existence or uniqueness of the singular value or polar decomposition although strictly speaking \mathbf{S} is not positive definite anymore.

The algorithm proceeds as follows:

1. **Symmetric eigenanalysis:** A Jacobi eigenvalue algorithm begins with the symmetric positive definite matrix $\mathbf{S}^{(0)} = \mathbf{A}^T \mathbf{A} = \mathbf{V} \mathbf{\Sigma}^2 \mathbf{V}^T$.
 - 1.1. Iteratively compute (an also symmetric, positive definite) $\mathbf{S}^{(k+1)} = [\mathbf{Q}^{(k)}]^T \mathbf{S}^{(k)} \mathbf{Q}^{(k)}$ where \mathbf{Q} is a Givens-Rotation aiming to eliminate off S_{12} . Store $\mathbf{V}^{(k+1)} = \mathbf{V}^{(k)} \mathbf{Q}^{(k)}$.
 - 1.2. Do 1.1. again for the other off-diagonal entries S_{13}, S_{23} .
 - 1.3. Redo 1.1. - 1.2. a fixed amount of steps m .
2. **Sorting singular values:** Compute $\mathbf{B} := \mathbf{A} \mathbf{V}$, where $\mathbf{V} = \mathbf{V}^{(3m)}$. Acquire $\mathbf{\Sigma}$ by $\|\mathbf{b}_i\|_2 = \|\mathbf{u}_i \sigma_i\|_2 = |\sigma_i|$, where also $\mathbf{B} = \mathbf{U} \mathbf{\Sigma}$ holds. Permute the singular values by sorting them in decreasing order. Apply the same permutation to the columns of \mathbf{B} and \mathbf{V} , where switches in \mathbf{V} also cause a sign change. Enforce the convention mentioned above.
3. **QR-factorization:** Compute \mathbf{U} using a \mathbf{QR} -factorization with Givens-Rotations where $\mathbf{B} = \mathbf{Q} \mathbf{R} = \mathbf{U} \mathbf{\Sigma}$. The \mathbf{QR} -factorization is done once in the same fashion as in item 1.1. - 1.2..

Due to inherent normalization, fast multiplication and storage efficiency quaternions are preferred over actual rotation matrices. In item 3 a \mathbf{QR} -factorization is preferred over a column normalization of $\mathbf{\Sigma} \mathbf{U}$ due to its inaccuracy at near-zero singular values. In general \mathbf{R} is an upper triangular matrix. In item 3 it reduces to being diagonal. [Jia+16][McA+11a]

4.3 Constitutive models

It is common practice in elastoplasticity theory to decompose the deformation gradient in its elastic and plastic parts $\mathbf{F} = \mathbf{F}_E \mathbf{F}_P$. The elastic part is recoverable. The plastic part is irreversibly lost. Plastic models are not covered here. They extend the energy densities discussed here with additional terms $\Psi(\mathbf{F}_E, \mathbf{F}_P)$. For more information refer to the literature [Öch14].

4.3.1 Linear elasticity

The first aim will be to find the strain energy density $\Psi(\epsilon)$ of the strain ϵ . The most general linear stress-strain relationship is given by Hooke's Law in three dimensions:

$$\sigma_{ij} = C_{ijkl} \epsilon_{kl}, \quad (31)$$

where σ and ϵ are second-order tensors with $(3 \times 3) = 9$ elements. C_{ijkl} is a fourth-order stiffness-tensor with $(3 \times 3) \times (3 \times 3) = 81$ elements. Assuming following symmetries reduces the tensors to 6 and 21 unique elements respectively:

1. Conservation of angular momentum: $\sigma_{ij} = \sigma_{ji} \Rightarrow C_{ijkl} = C_{jikl}$.
2. No-net-rotation: $\epsilon_{kl} = \epsilon_{lk} \Rightarrow C_{ijkl} = C_{ijlk}$.
3. Equivalence of second-order mixed partials of Ψ :

$$C_{ijkl} = \frac{\partial^2 \Psi}{\partial \epsilon_{kl} \partial \epsilon_{ij}} = \frac{\partial^2 \Psi}{\partial \epsilon_{ij} \partial \epsilon_{kl}} = C_{klij}, \quad (32)$$

where item 3 holds for the strain energy density functional of an (hyper-)elastic material. This potential Ψ is thus similar to potentials for example involved in gravitation, electrodynamics or fluids. The stress may then also be calculated by

$$\sigma_{ij} = \sigma_{ij}(\epsilon) = \frac{\partial \Psi}{\partial \epsilon_{ij}}, \quad (33)$$

if such a Ψ is given. An isotropic (direction-independent) linear elastic material further only has three unique elements C_{ijkl} . Using Voigt-Notation, which collapses indices $i = j$ and $k = l$, equation 31 can be rewritten as:

$$\begin{bmatrix} \sigma_{11} \\ \sigma_{22} \\ \sigma_{33} \\ \sigma_{23} \\ \sigma_{13} \\ \sigma_{12} \end{bmatrix} = \begin{bmatrix} C_{11} & C_{12} & C_{12} & 0 & 0 & 0 \\ & C_{11} & C_{12} & 0 & 0 & 0 \\ & & C_{11} & 0 & 0 & 0 \\ & & & C_{22} & 0 & 0 \\ & & & & C_{22} & 0 \\ sym & & & & & C_{22} \end{bmatrix} \begin{bmatrix} \epsilon_{11} \\ \epsilon_{22} \\ \epsilon_{33} \\ \gamma_{23} \\ \gamma_{13} \\ \gamma_{12} \end{bmatrix}. \quad (34)$$

Experimental results of Hooke's law commonly give

$$\epsilon = \epsilon_{ij} = \frac{1}{E} [(1 + \nu)\sigma_{ij} - \nu\sigma_{kk}\delta_{ij}] = C^{-1}\sigma \quad (35)$$

using engineering constants Young's modulus E and Poisson ratio ν . Inverting C^{-1} and switching to Lamé parameters λ and μ results in the equation:

$$\sigma_{ij} = 2\mu\epsilon_{ij} + \lambda\text{tr}(\epsilon)\delta_{ij}. \quad (36)$$

Comparing with equation 34 leads to coefficients $\gamma_{ij} = 2\epsilon_{ij}$ for $(i \neq j)$, $C_{11} = \lambda + 2\mu$, $C_{12} = \lambda$, and $C_{22} = \mu$. γ is also referred to as the engineering strain. Due to the relationship in 33 the model for linear elasticity in terms of the strain energy density function Ψ_{LE} after integration of 36 concludes to:

$$\Psi_{LE} = \mu\|\epsilon\|_F^2 + \frac{\lambda}{2}\text{tr}^2(\epsilon). \quad (37)$$

[AER]

4.3.2 Corotated hyperelasticity

The simplest tensor assumed by infinitesimal strain theory is the small strain tensor:

$$\epsilon_l = \frac{1}{2} \left(\mathbf{F}_E + \mathbf{F}_E^T \right) - \mathbf{I}. \quad (38)$$

The energy produced by equation 37 using the small strain tensor is not rotationally invariant w.r.t. to \mathbf{F}_E : $\Psi_{LE}(\epsilon_l(\mathbf{R}_0 \mathbf{F}_E)) \neq \Psi_{LE}(\epsilon_l(\mathbf{F}_E))$. Rigid body motions however don't result in strain and consequently don't need to be recovered from. So energy should not change. Given the polar decomposition $\mathbf{F}_E = \mathbf{R}_E \mathbf{S}_E$ an alternate strain measure may be defined as:

$$\epsilon(\mathbf{F}_E) = \epsilon_l \left(\mathbf{R}_E^T \mathbf{F}_E \right) = \frac{1}{2} \left(\mathbf{R}_E^T \mathbf{F}_E + \left(\mathbf{R}_E^T \mathbf{F}_E \right)^T \right) - \mathbf{I} = \mathbf{S}_E - \mathbf{I}. \quad (39)$$

Substituting ϵ into equation 37 leads to the energy definition of corotational hyperelasticity:

$$\Psi_{CH} = \mu \|\mathbf{S}_E - \mathbf{I}\|_F^2 + \frac{\lambda}{2} \text{tr}^2(\mathbf{S}_E - \mathbf{I}). \quad (40)$$

Using rotation-invariance of the Frobenius norm:

$$\Psi_{CH} = \mu \|\mathbf{F}_E - \mathbf{R}_E\|_F^2 + \frac{\lambda}{2} \text{tr}^2 \left(\mathbf{R}_E^T \mathbf{F}_E - \mathbf{I} \right) \quad (41)$$

Even more insight yields the relationship to their singular values σ_i , also called the principal stretches:

$$\begin{aligned} \text{tr}(\mathbf{S}) &= \sum_{i=1} \sigma_i = \text{tr}(\mathbf{\Sigma}_E) \\ \|\mathbf{S}_E\|_F^2 &= \sum_{i=1} \sigma_i^2 = \|\mathbf{\Sigma}_E\|_F^2 \\ \Rightarrow \|\mathbf{S}_E - \mathbf{I}\|_F^2 &= \|\mathbf{S}_E\|_F^2 - 2 \text{tr}(\mathbf{S}_E) + \|\mathbf{I}\|_F^2 = \|\mathbf{\Sigma}_E - \mathbf{I}\|_F^2 \\ \Psi_{CH}(\mathbf{\Sigma}_E) &= \mu \|\mathbf{\Sigma}_E - \mathbf{I}\|_F^2 + \frac{\lambda}{2} \text{tr}^2(\mathbf{\Sigma}_E - \mathbf{I}) \end{aligned} \quad (42)$$

Equation 42 uses the diagonal matrix $\mathbf{\Sigma}_E$ containing the principal stretches typically acquired by the singular value decomposition $\mathbf{F}_E = \mathbf{U} \mathbf{\Sigma}_E \mathbf{V}^T$. Since the energy density in 42 is a function of only three (singular) values, which describe stretch/compression of the material, isotropy of the material is underlined.

[McA+11b]

4.3.3 Fixed corotated hyperelasticity

Numerical implicit stepping algorithms mostly rely on using the first and second derivative of Ψ , chapter 4.6.6. Furthermore one may describe an isotropic elastic model due to their principal stretches $\sigma_1, \sigma_2, \sigma_3$, chapter 4.2. The rest configuration is reached, when $\sigma_1, \sigma_2, \sigma_3 = 1$. I.e. no elastic forces will be exerted because the material is completely relaxed (again).

Under material relaxation these stepping algorithms are attracted to a material-dependent primary contour. For instance for a model that aims for high volume preservation (Poisson ratio $\nu = 0.5$) the primary contour is primarily enforcing volume preservation ($J_E = \sigma_1 \sigma_2 \sigma_3 \approx 1$). Reaching the rest configuration is only the secondary goal.

The primary contour can be formalized as $\mathbf{v} \cdot \mathbf{g} = 0$ of the gradient $g_i = \frac{\partial \Psi}{\partial \sigma_i}$ and the eigenvector with the largest-magnitude eigenvalue \mathbf{v} of the Hessian $H_{ij} = \frac{\partial^2 \Psi}{\partial \sigma_i \partial \sigma_j}$. Problems arise in Ψ_{CH} as the primary contour can easily cross into the inverted region ($\sigma_3 < 0$) leading to inverted configurations while relaxing. This is undesired behavior. Furthermore, the primary contour can lead into energy kinks at extreme stretches leading to oscillations.

Therefore, they propose to use the fixed corotated hyperelasticity energy density:

$$\Psi_{FCH} = \mu \|\boldsymbol{\Sigma}_E - \mathbf{I}\|_F^2 + \frac{\lambda}{2} (J_E - 1)^2. \quad (43)$$

This leads to the primary contour $J = 1$ which does not cross the inverted region as only one singular value may be negative.

[Sto+12]

4.4 Governing equations

Starting from the governing equations this chapter will lead to the weak formulation core of any finite element and material point method.

4.4.1 Conservation of mass

Let the Eulerian mass density be ${}_t\rho({}_t\mathbf{x}, t)$. Similarly, let its (Lagrangian) pull back be ${}_0\rho({}_0\mathbf{x}, t)$. After 23 they are related as:

$$\int_{{}_tB_\epsilon} {}_t\rho({}_t\mathbf{x}, t) d{}_t\mathbf{x} = \int_{{}_0B_\epsilon} {}_0J {}_0\rho({}_0\mathbf{x}, t) d{}_0\mathbf{x}. \quad (44)$$

An open ball ${}_0B_\epsilon$ in the reference configuration will have the same mass as its respective open ball ${}_tB_\epsilon$ in the current configuration. Keep in mind that both refer to a deformed state.

Conservation of mass dictates that mass does not depend on motion or time. Only the space occupied by this mass may be more or less.

$$\frac{d}{dt} \int_{_t B_\epsilon} {}_t \rho({}_t \mathbf{x}, t) d{}_t \mathbf{x} = 0 \quad (45)$$

Equivalently this can be formulated with the constant undeformed initial mass in Lagrangian view:

$$\left(\int_{_t B_\epsilon} {}_t \rho({}_t \mathbf{x}, t) d{}_t \mathbf{x} \stackrel{44}{=} \right) \int_{_0 B_\epsilon} {}_0 J {}_0 \rho({}_0 \mathbf{x}, t) d{}_0 \mathbf{x} = \int_{_0 B_\epsilon} {}_0 \rho({}_0 \mathbf{x}, 0) d{}_0 \mathbf{x}. \quad (46)$$

In Eulerian view the conservation of mass is more difficult to develop and starts with the Lagrangian view. Since the integrals do account for arbitrary volumes, they are left out in the following:

$$\frac{\partial}{\partial t} ({}_0 \rho {}_0 J) = \frac{\partial {}_0 \rho}{\partial t} {}_0 J + \frac{\partial {}_0 J}{\partial t} {}_0 \rho = 0. \quad (47)$$

The left side could be immediately pushed forward, the right side is harder:

$$\frac{\partial J}{\partial t} = \frac{\partial J}{\partial F_{ij}} \frac{\partial F_{ij}}{\partial t} \stackrel{49,50}{=} J F_{ji}^{-1} \frac{\partial v_i}{\partial x_k} F_{kj} = J \delta_{ik} \frac{\partial v_i}{\partial x_k} = J \frac{\partial v_i}{\partial x_i}. \quad (48)$$

The determinant differentiation rule can be shown by expressing the determinant with Laplace's expansion and applying the derivative on it:

$$\frac{\partial J}{\partial F_{ij}} = \frac{\partial (F_{ik} \text{adj}(F)_{ki})}{\partial F_{ij}} = \text{adj}(F)_{ji} = J F_{ji}^{-1}. \quad (49)$$

The time-evolution of the deformation gradient is:

$$\frac{\partial {}_0 F_{ij}}{\partial t} = \frac{\partial}{\partial t} \frac{\partial {}_0 \phi_i}{\partial {}_0 x_j}({}_0 \mathbf{x}, t) = \frac{\partial {}_0 v_i}{\partial {}_0 x_j}({}_0 \mathbf{x}, t) = \frac{\partial {}_t v_i}{\partial {}_t x_k}({}_t \phi({}_0 \mathbf{x}, t), t) \frac{\partial {}_t x_k}{\partial {}_0 x_j}({}_0 \mathbf{x}, t). \quad (50)$$

Pushing forward 47 with the result of 48 using the material derivative formulation 20 leads to the Eulerian conservation of mass:

$$\frac{D}{Dt} \rho({}_t \mathbf{x}, t) + \rho({}_t \mathbf{x}, t) \vec{\nabla} \cdot \mathbf{v}({}_t \mathbf{x}, t) = 0. \quad (51)$$

Commonly used is the Nabla operator: $\vec{\nabla} = \left(\frac{\partial}{\partial x_1}, \dots, \frac{\partial}{\partial x_n} \right)$. [Jia+16]

4.4.2 Conservation of momentum

Continuum forces are divided up into body and surface forces. A surface force acts upon the surface of the material $\partial_t B_\epsilon$. While a body force scales upon the volume

of the material ${}_tB_\epsilon$. Conservation of momentum may then be expressed in a similar way to the conservation of mass as:

$$\frac{d}{dt} \int_{{}_tB_\epsilon} \rho({}_t\mathbf{x}, t) \mathbf{v}({}_t\mathbf{x}, t) d_t\mathbf{x} = \int_{\partial_t B_\epsilon} \boldsymbol{\sigma} d_t\mathbf{A}({}_t\mathbf{x}) + \int_{{}_tB_\epsilon} \mathbf{f}^{\text{body}} d_t\mathbf{x}. \quad (52)$$

Already assumed is angular momentum conservation $\boldsymbol{\sigma}^T = \boldsymbol{\sigma}$ out of the second part of this section. Beginning with a mix out of Lagrangian and Eulerian view

$$\begin{aligned} & \left(\frac{d}{dt} \int_{{}_tB_\epsilon} \rho({}_t\mathbf{x}, t) \mathbf{v}({}_t\mathbf{x}, t) d_t\mathbf{x} \stackrel{19}{=} \right) \frac{d}{dt} \int_{{}_0B_\epsilon} {}_0J \rho({}_0\mathbf{x}, t) \mathbf{v}({}_0\mathbf{x}, t) d_0\mathbf{x} \\ & \stackrel{47}{=} \int_{{}_0B_\epsilon} {}_0J \rho({}_0\mathbf{x}, t) \mathbf{a}({}_0\mathbf{x}, t) d_0\mathbf{x} = \int_{\partial_t B_\epsilon} \boldsymbol{\sigma} d_t\mathbf{A}({}_t\mathbf{x}) + \int_{{}_tB_\epsilon} \mathbf{f}^{\text{body}} d_t\mathbf{x} \end{aligned} \quad (53)$$

where conservation of mass (equation 47) was applied. The Eulerian push-forward of the left side combined with the divergence theorem becomes:

$$\int_{{}_tB_\epsilon} \rho({}_t\mathbf{x}, t) \mathbf{a}({}_t\mathbf{x}, t) d_t\mathbf{x} = \int_{\partial_t B_\epsilon} \vec{\nabla} \cdot \boldsymbol{\sigma} d_t\mathbf{x} + \int_{{}_tB_\epsilon} \mathbf{f}^{\text{body}} d_t\mathbf{x}. \quad (54)$$

The acceleration ${}_t\mathbf{a}$ is again defined due to the material derivative 20. Thus the Eulerian momentum balance equation becomes:

$${}_t\rho \frac{D_t\mathbf{v}}{Dt} = \vec{\nabla} \cdot \boldsymbol{\sigma} + \mathbf{f}^{\text{body}}. \quad (55)$$

There is a quantity left to be defined for the Lagrangian view. The Cauchy stress $\boldsymbol{\sigma}$ is defined in the current configuration. Pulling back the Cauchy stress leads to a stress measure named the first Piola Kirchhoff stress

$$\int_{\partial_t B_\epsilon} {}_t\boldsymbol{\sigma} d_t\mathbf{A}({}_t\mathbf{x}) \stackrel{26}{=} \int_{\partial_0 B_\epsilon} {}_0\boldsymbol{\sigma} \mathbf{F}^{-T} J d_0\mathbf{A}({}_0\mathbf{x}) = \int_{\partial_0 B_\epsilon} \mathbf{P} d_0\mathbf{A}({}_0\mathbf{x}), \quad (56)$$

denoted in the literature as:

$$\mathbf{P} = \frac{\partial \Psi}{\partial \mathbf{F}} = \boldsymbol{\sigma} \mathbf{F}^{-T} J. \quad (57)$$

Summarized, the Lagrangian view of the momentum equation with an initial momentum is (${}_0J = 1$):

$${}_0\rho({}_0\mathbf{x}, 0) {}_0\mathbf{a}({}_0\mathbf{x}, t) = \vec{\nabla} \cdot \mathbf{P}({}_0\mathbf{x}, t) + {}_0\mathbf{f}^{\text{body}}({}_0\mathbf{x}, t) {}_0J. \quad (58)$$

For the stress strain relationship \mathbf{C} in chapter 4.3.1 as well as the start of this chapter conservation of angular momentum caused $\sigma_{ij} = \sigma_{ji}$. This can be shown as follows. The description of angular momentum follows that of linear momentum (${}_t\mathbf{x} \times 54$) where product rule generally applies $\left(\frac{D_t\mathbf{x}}{Dt} \times {}_t\mathbf{v} = {}_t\mathbf{v} \times {}_t\mathbf{v} = 0 \right)$:

$$\int_{{}_tB_\epsilon} {}_t\mathbf{x} \times \rho({}_t\mathbf{x}, t) \mathbf{a}({}_t\mathbf{x}, t) d_t\mathbf{x} = \int_{\partial_t B_\epsilon} {}_t\mathbf{x} \times \boldsymbol{\sigma}^T d_t\mathbf{A}({}_t\mathbf{x}) + \int_{{}_tB_\epsilon} {}_t\mathbf{x} \times \mathbf{f}^{\text{body}} d_t\mathbf{x}. \quad (59)$$

In component form this becomes:

$$\int_{tB_\epsilon} \varepsilon_{ijk} \rho x_j a_k d_t \mathbf{x} = \int_{\partial_t B_\epsilon} \varepsilon_{ijk} x_j \sigma_{mk} dA_m(t\mathbf{x}) + \int_{tB_\epsilon} \varepsilon_{ijk} x_j f_k^{\text{body}} d_t \mathbf{x}. \quad (60)$$

The divergence theorem is again applied to the surface forces $\left(\vec{\nabla} = \frac{\partial}{\partial x_m}\right)$:

$$\begin{aligned} \int_{\partial_t B_\epsilon} \varepsilon_{ijk} x_j \sigma_{mk} dA_m(t\mathbf{x}) &= \int_{tB_\epsilon} \varepsilon_{ijk} \frac{\partial(x_j \sigma_{mk})}{\partial x_m} d_t \mathbf{x} \\ &= \int_{tB_\epsilon} \varepsilon_{ijk} \left(\delta_{jm} \sigma_{mk} + x_j \frac{\partial \sigma_{mk}}{\partial x_m} \right) d_t \mathbf{x}. \end{aligned} \quad (61)$$

The conservation of momentum (equation 54) can then be applied to the result of plugging 61 back into 60 leaving only:

$$\int_{tB_\epsilon} \varepsilon_{ijk} \sigma_{jk} d_t \mathbf{x} = 0. \quad (62)$$

Leaving out the integral and multiplying by ε_{irs} enables equation 12. The Cauchy stress is constrained to

$$\sigma_{ij} = \sigma_{ji} \quad (63)$$

as assumed before. Note that \mathbf{P} however is not constrained to be symmetric.

[Jia+16][Abe12]

4.4.3 Weak formulation

Before deriving the weak form an explanation of what it achieves is in order. The previous presented governing equations are written in the strong form: a solution to the equation needs to be exact on the whole domain and is as such influenced by the whole domain in general. Such a solution can be found for simplified models analytically. These act as a ground truth to numerical methods like the material point method. Analytical methods of today can't handle complex problems: Numerical solutions try to overcome that hurdle.

The complete mathematical description of the weak formulation is beyond this thesis. Numeric books that discuss finite element methods will provide one ([Bat06], [DR08]). For simplicity: The weak formulation combined with Galerkin discretization restricts the globality of the strong method due to so called 'test functions': ${}_0\mathbf{q}_h$. A 'test function' generally only has limited support, i.e. ${}_0\mathbf{q}_h \neq 0$ on a very small subset of the whole domain Ω^0 . This is mostly used to gather information on a local neighborhood and not on the whole domain.

The weak formulation requires an observation of the dot product. Consider the conservation of momentum in the strong form as formulated before 58 as:

$${}_0\rho({}_0\mathbf{x}, 0){}_0\mathbf{a}({}_0\mathbf{x}, t) = \vec{\nabla} \cdot \mathbf{P}({}_0\mathbf{x}, t) + {}_0\mathbf{f}^{\text{body}}({}_0\mathbf{x}, t) {}_0^t J. \quad (64)$$

Multiply both sides with the dot product of an arbitrary function ${}_0\mathbf{q}(\cdot, t) : \Omega^0 \rightarrow \mathbb{R}^d$ and integrate over Ω^0 . If a solution solves the balance of 64 then it also solves:

$$\begin{aligned} \int_{\Omega^0} {}_0q_i(\mathbf{x}, t) \left({}_0\rho(\mathbf{x}, 0){}_0a_i(\mathbf{x}, t) - {}_0\mathbf{f}^{\text{body}}(\mathbf{x}, t){}_0^tJ \right) d\mathbf{x} \\ = \int_{\Omega^0} {}_0q_i(\mathbf{x}, t) \frac{\partial P_{ij}}{\partial x_j}(\mathbf{x}, t) d\mathbf{x}. \end{aligned} \quad (65)$$

With the help of partial integration in multiple dimension, the derivative moves over to the test-function. Balancing out the order of derivatives, by moving a derivative to the test function, is the main motive of the weak form:

$$\int_{\Omega^0} \frac{\partial({}_0q_i(\mathbf{x}, t)P_{ij}(\mathbf{x}, t))}{\partial {}_0x_j} - \frac{\partial {}_0q_i}{\partial {}_0x_j}(\mathbf{x}, t)P_{ij}(\mathbf{x}, t) d\mathbf{x}.$$

The divergence theorem allows to convert the first term to a boundary integral.

$$\int_{\partial\Omega^0} {}_0q_i(\mathbf{x}, t)P_{ij}(\mathbf{x}, t)d{}_0\mathbf{A}(\mathbf{x}) - \int_{\Omega^0} \frac{\partial {}_0q_i}{\partial {}_0x_j}(\mathbf{x}, t)P_{ij}(\mathbf{x}, t)d\mathbf{x}. \quad (66)$$

Mathematically the boundary integral serves as a boundary condition which is set by the specific problem (e.g. context of the simulation). Finally putting together the previous results gives the weak form of force balance in the Lagrangian view:

$$\begin{aligned} \int_{\Omega^0} {}_0q_i(\mathbf{x}, t) \left({}_0\rho(\mathbf{x}, 0){}_0a_i(\mathbf{x}, t) - {}_0\mathbf{f}_i^{\text{body}}(\mathbf{x}, t){}_0^tJ \right) d\mathbf{x} \\ = \int_{\partial\Omega^0} {}_0q_i(\mathbf{x}, t)P_{ij}(\mathbf{x}, t)d{}_0\mathbf{A}(\mathbf{x}) - \int_{\Omega^0} \frac{\partial {}_0q_i}{\partial {}_0x_j}(\mathbf{x}, t)P_{ij}(\mathbf{x}, t)d\mathbf{x}. \end{aligned} \quad (67)$$

In the material point method stress computations are more naturally done in the current configuration or equally in terms of the Cauchy stress as seen in chapter 4.3.1. Pushing the equation forward to Eulerian view with the push forward ${}_t\mathbf{q} : \Omega^t \rightarrow \mathbb{R}^d$ of ${}_0\mathbf{q}$ is only a problem for the last term:

$$\begin{aligned} \int_{\Omega^0} \frac{\partial {}_0q_i}{\partial {}_0x_j}(\mathbf{x}, t)P_{ij}d\mathbf{x} \stackrel{57, 23}{=} \int_{\Omega^0} \left({}_tF_{kj} \frac{\partial {}_tq_i}{\partial {}_tx_k}({}_t\mathbf{x}, t) \right) \left({}_tF_{kj}\sigma_{ik}{}_t^tJ \right) d{}_t\mathbf{x} \\ = \int_{\Omega^t} \frac{\partial {}_tq_i}{\partial {}_tx_k}({}_t\mathbf{x}, t)\sigma_{ik}d{}_t\mathbf{x}. \end{aligned} \quad (68)$$

This completes the Eulerian view to be:

$$\begin{aligned} \int_{\Omega^t} {}_tq_i({}_t\mathbf{x}, t) \left({}_t\rho({}_t\mathbf{x}, t){}_ta_i({}_t\mathbf{x}, t) - {}_tf_i^{\text{body}}({}_t\mathbf{x}, t) \right) d{}_t\mathbf{x} \\ = \int_{\partial\Omega^t} {}_tq_i({}_t\mathbf{x}, t)\sigma_{ij}d{}_tA_j({}_t\mathbf{x}) - \int_{\Omega^t} \frac{\partial {}_tq_i}{\partial {}_tx_k}({}_t\mathbf{x}, t)\sigma_{ik}d{}_t\mathbf{x}. \end{aligned} \quad (69)$$

[Jia+16][Str07][Bat06]

4.5 Material point method

The key idea of the material point method is to use (Lagrangian) particles as a consistent storage of material properties. All stress based forces are computed on a Eulerian grid however. This grid does not store any material properties and is therefore often referred to as a scratch pad.

As a corollary there needs to be a way to transfer information from a particle to the neighboring grid cells. This also induces switching from Lagrangian to Eulerian view. After stresses are computed there also needs to be a way to get back the relevant information from the grid to the particles. Advection is typically hard to do in Eulerian/FE-like methods and cause of a lot of problems down the development pipeline. In a Lagrangian view particle advection is trivial.

It is very important that the two transfers as well as the grid solver are in compliance with all governing equations. While the grid solver will be derived from the weak form of the governing equation the transfers also need to be chosen in a way that conserve the properties defined in them. [Jia+16]

4.5.1 Interpolation weights

The choice of interpolation weights is flexible. Nevertheless a kernel $w(\mathbf{x})$ requires some important properties to be qualified for MPM:

1. Partition of unity:

$$\sum_i w(\mathbf{x} - \mathbf{x}_i^n) = 1. \quad (70)$$

2. Identity relation:

$$\sum_i \mathbf{x}_i^n w(\mathbf{x} - \mathbf{x}_i^n) = \mathbf{x}. \quad (71)$$

3. Non-negativity: $w \geq 0$. Negative weights can cause severe instability or non-physical behavior, unlike in FEM where they are used. [Gao+17]
4. Limited local support to reduce the number of discretizations, chapter 4.6.
5. C^1 -continuity s.t. ∇w is continuous.

As a reminder of chapter 3: \mathbf{x}_p refers to a particle's position. \mathbf{x}_i to a grid cell's position. For a more general discussion refer to [Gao+17]. Often dyadic products of one-dimensional interpolation functions suffice

$$w(\mathbf{x} - \mathbf{x}_i^n) = w_i^n(\mathbf{x}) = w\left(\frac{1}{h}(x - x_i^n)\right) w\left(\frac{1}{h}(y - y_i^n)\right) w\left(\frac{1}{h}(z - z_i^n)\right) \quad (72)$$

$$\nabla w_i^n(\mathbf{x}) = \frac{1}{h} \begin{pmatrix} w'(\frac{1}{h}(x - x_i^n))w(\frac{1}{h}(y - y_i^n))w(\frac{1}{h}(z - z_i^n)) \\ w(\frac{1}{h}(x - x_i^n))w'(\frac{1}{h}(y - y_i^n))w(\frac{1}{h}(z - z_i^n)) \\ w(\frac{1}{h}(x - x_i^n))w(\frac{1}{h}(y - y_i^n))w'(\frac{1}{h}(z - z_i^n)) \end{pmatrix} \quad (73)$$

where h is the grid spacing (of a uniform grid). An interpolation function often employed is a cubic B-spline (C^2):

$$w(x) = \begin{cases} \frac{1}{2}|x|^3 - |x|^2 + \frac{2}{3} & 0 \leq |x| < 1 \\ \frac{1}{6}(2 - |x|)^3 & 1 \leq |x| < 2 \\ 0 & 2 \leq |x| \end{cases} . \quad (74)$$

Since these function are used to weight (or filter) particles a shortening in notation may be employed as $w_{ip}^n = w(\mathbf{x}_p^n - \mathbf{x}_i^n)$. [JST17][Jia+16][SKB08][Gao+17]

4.5.2 Mass transfer

Each material point will be assigned an initial volume ${}_0V_p$ as well as an initial mass ${}_0m_p$. The volume the material point occupies may change in time due to equation 24: ${}_0J_0V_p = {}_tV_p$. But, due to conservation of mass 46 it will have a constant, initial mass associated with it. I.e. there will only be a transfer to the grid and no transfer back. A transfer of mass to the grid may then be expressed as:

$$m_i = \sum_p w_{ip} m_p. \quad (75)$$

$\sum_i m_i = \sum_p m_p$ is a complete prove this fulfills the conservation of mass. Remember there is no transfer back. In doing so no information can be lost on the particles. Proving that the mass transfer to the grid is conserving is enough. The stress based-solver may manipulate this information further. Mass-lumping strategies typically will use this information directly, equation 102.

$$\sum_i m_i \stackrel{75}{=} \sum_i \sum_p w_{ip} m_p = \sum_p m_p \sum_i w_{ip} \stackrel{70}{=} \sum_p m_p \quad (76)$$

[JST17][Jia+16]

4.5.3 APIC-transfers

The momentum transfer round trip could be defined as:

1. Particle to grid momentum transfer:

$$(m\mathbf{v})_i^n = \sum_p w_{ip} m_p \mathbf{v}_p^n. \quad (77)$$

2. Factoring out mass:

$$\mathbf{v}_i^n = \frac{(m\mathbf{v})_i^n}{m_i^n}. \quad (78)$$

3. Coupled with either ($\alpha \in \{0, 1\}$) or a combination ($\alpha \in]0; 1[$) of:

$$\mathbf{v}_p^{n+1} = \alpha \mathbf{v}_{p,PIC}^{n+1} + (1 - \alpha) \mathbf{v}_{p,FLIP}^{n+1} \quad (79)$$

$$\mathbf{v}_{p,PIC}^{n+1} = \sum_i w_{ip} \mathbf{v}_i^{n+1}. \quad (80)$$

$$\mathbf{v}_{p,FLIP}^{n+1} = \mathbf{v}_p^n + \sum_i w_{ip} (\mathbf{v}_i^{n+1} - \mathbf{v}_i^n). \quad (81)$$

While *PIC*-transfers are very stable, they suffer from excessive (energy) dissipation due to double interpolating on the whole quantity 77,80. This causes a heavy loss in angular momentum and velocity modes. *FLIP*-Transfers avoid dissipation and loss of angular momentum by only updating the velocity with a difference 81. However, some velocity modes are also not recognized on the grid and may cause unpredictable and unstable behavior in following steps. Therefore, often a combination of both is taken.

APIC builds on top of the very stable *PIC*-transfers and effectively only adds an extra term of the Taylor series to increase accuracy. This extra term \mathbf{C}_p may be in short just referred to as the velocity derivative. The local velocity field around a particle may then be characterized by the affine function $\mathbf{v}(\mathbf{x}) = \mathbf{C}_p(\mathbf{x} - \mathbf{x}_p)$.

Motivated by the theory of angular momentum and moment of inertia one can define a quantity

$$\mathbf{D}_p^n = \sum_i w_{ip}^n (\mathbf{x}_i^n - \mathbf{x}_p^n)(\mathbf{x}_i^n - \mathbf{x}_p^n)^T \quad (82)$$

which is similar to the classically known inertia tensor:

$$\begin{aligned} \mathbf{I}_p &= - \sum_i m_i [\mathbf{x}_i - \mathbf{x}_p][\mathbf{x}_i - \mathbf{x}_p]^T \\ &= \sum_i m_i ((\mathbf{x}_i - \mathbf{x}_p)^T (\mathbf{x}_i - \mathbf{x}_p) \mathbf{I} - (\mathbf{x}_i - \mathbf{x}_p)(\mathbf{x}_i - \mathbf{x}_p)^T) \end{aligned} \quad (83)$$

Bearing in mind, that \mathbf{D}_p^n does not include a mass and is defined for an affine motion instead of an angular motion where $[a]_{\alpha\gamma} = \varepsilon_{\alpha\beta\gamma} a_\beta$ is the cross-product matrix and \mathbf{I} denotes the identity matrix. In classical mechanics the angular velocity $\boldsymbol{\omega}_p$ can be then described using the inertia tensor \mathbf{I}_p with the help of the angular momentum \mathbf{L}_p :

$$\boldsymbol{\omega}_p = \mathbf{I}_p^{-1} \mathbf{L}_p. \quad (84)$$

This motivates the velocity derivative to be equally defined by a similar relationship where \mathbf{B}_p^n holds momentum information.

$$\mathbf{C}_p^n = (\mathbf{D}_p^n)^{-1} \mathbf{B}_p^n. \quad (85)$$

The transfers of the *APIC* scheme are then summarized:

1. Particle to grid:

$$(m\mathbf{v})_i^n = \sum_p w_{ip}^n m_p (\mathbf{v}_p^n + \mathbf{B}_p^n (\mathbf{D}_p^n)^{-1} (\mathbf{x}_i^n - \mathbf{x}_p^n)) \quad (86)$$

2. Factoring out mass:

$$\mathbf{v}_i^n = \frac{(m\mathbf{v})_i^n}{m_i^n}. \quad (87)$$

3. Grid to particle transfer (in a *PIC* manner), where in contrast the new particle position \mathbf{x}_p also needs to be interpolated:

$$\mathbf{x}_p^{n+1} = \sum_i w_{ip} \mathbf{x}_i^{n+1} \quad (88)$$

$$\mathbf{v}_p^{n+1} = \sum_i w_{ip} \mathbf{v}_i^{n+1} \quad (89)$$

$$\begin{aligned} -\Delta \mathbf{x} &= \mathbf{x}_i^n - \mathbf{x}_p^n + \mathbf{x}_i^{n+1} - \mathbf{x}_p^{n+1}, \quad +\Delta \mathbf{x} = \mathbf{x}_i^n - \mathbf{x}_p^n - \mathbf{x}_i^{n+1} + \mathbf{x}_p^{n+1} \\ \mathbf{B}_p^{n+1} &= \frac{1}{2} \sum_i w_{ip}^n (\mathbf{v}_i^{n+1} (-\Delta \mathbf{x})^T + \mathbf{v}_i^{n+1} \Delta \mathbf{x} (\mathbf{v}_i^{n+1})^T). \end{aligned} \quad (90)$$

For a full proof, that these transfers preserve linear and angular momentum, consult [JST17]. For the choice of dyadic products of cubic b-splines (74) \mathbf{D}_p takes on the simple form:

$$\mathbf{D}_p^n = \frac{1}{3} h^2 \mathbf{I}. \quad (91)$$

A simple proof (Appendices: A) cancelling out the numerous polynomials can be done for instance using SymPy ([Sym]).[JST17][Jia+15]

4.5.4 CFL condition

The CFL condition is prominent for FEM: For a stable integration a particle should not travel farther than the grid spacing h in a discrete time-step Δt . Δt is thus limited by:

$$\Delta t \leq \frac{h}{\|\mathbf{v}_i^n\|_2}. \quad (92)$$

Assuming $\|\mathbf{x}_i^n - \mathbf{x}_p^n\| \leq \kappa h$, where κ is determined by the interpolation stencil support (cubic 3D: $\kappa = 2\sqrt{3}$) and additionally assuming $\mathbf{D}_p^n = k\mathbf{I} \Rightarrow (\mathbf{D}_p^n)^{-1} = \frac{1}{k}\mathbf{I}$ (cubic 3D: $k = \frac{1}{3}h^2$), $\|\mathbf{v}_i^n\|_2$ can be estimated on the particles. Typically the number of particles is lower. Given Eq. 86 this leads to the following estimate:

$$\begin{aligned} \|\mathbf{v}_i^n\|_2 &\leq \frac{1}{m_i^n} \left(\sum_p w_{ip}^n m_p \|\mathbf{v}_p^n\|_2 + \sum_p w_{ip}^n m_p \|\mathbf{B}_p^n\|_F \|(\mathbf{D}_p^n)^{-1} (\mathbf{x}_i^n - \mathbf{x}_p^n)\|_2 \right) \\ &\leq \max_p (\|\mathbf{v}_p^n\|_2 + \frac{\kappa}{k} \Delta x \|\mathbf{B}_p^n\|_F) \end{aligned} \quad (93)$$

[JST17]

4.6 Discretization

The weak form of the force-balance in (67,69) implies the following, for MPM preferable, description:

$$\int_{\Omega^0} ({}_0q_\alpha)({}_0\rho_0)({}_0a_\alpha)d_0\mathbf{x} = \int_{\partial\Omega^{t^n}} {}_tq_\alpha\sigma_{\alpha\beta}d_tA_\beta({}_t\mathbf{x}) - \int_{\Omega^{t^n}} \frac{\partial {}_tq_\alpha}{\partial {}_tx_\beta}\sigma_{\alpha\beta}d_t\mathbf{x}. \quad (94)$$

The boundary integral is mostly due to collisions and will be ignored. [Gas+15] discuss level set collisions due to constraint collisions, object penalty collision and penalty self-collisions. Collision treatment would need to be involved in the solving of the equation. A simple though less accurate method is to process particle collisions separately in a typical computer graphics manner which is assumed for now.

4.6.1 Discretize time

Any integrator conserving linear and angular momentum could be used to discretize time. The class of time integrators used here are characterized by

$$\frac{y^{n+1} - y^n}{\Delta t} = f^{n+\lambda} = f\left(t^n + \lambda\Delta t, (1 - \lambda)y^n + \lambda y^{n+1}\right) \quad (95)$$

for a differential equation of order one:

$$\frac{\partial y}{\partial t}(t) = f(t, y(t)), \quad y(0) = y_0. \quad (96)$$

A prominent member of this class is the implicit midpoint rule ($\lambda = \frac{1}{2}$). Replacing the Lagrangian acceleration ${}_0a_\alpha$ in equation 94 with the left side of 95 using velocity, taking care of the right side and pushing forward to Eulerian view:

$$\frac{1}{\Delta t} \int_{\Omega^{t^n}} ({}_tq_\alpha)({}_t\rho)({}_tv_\alpha^{n+1} - {}_tv_\alpha^n)d_t\mathbf{x} = - \int_{\Omega^{t^n}} \frac{\partial {}_tq_\alpha}{\partial {}_tx_\beta}\sigma_{\alpha\beta}^{n+\lambda}d_t\mathbf{x}. \quad (97)$$

4.6.2 Discretize space

A Galerkin discretization brings all spatial terms of equation 97 to a finite-dimensional space: $\mathbf{q} \rightarrow \mathbf{q}_h$. To not further clutter up the notation, the h will be omitted. This will replace $q_\alpha, v_\alpha^n, v_\alpha^{n+1}$ with their finite-dimensional grid-based interpolants:

$${}_tq_\alpha^n = ({}_tq_{i\alpha}^n)({}_tw_i), \quad {}_tv_\alpha^n = ({}_tv_{j\alpha}^n)({}_tw_j), \quad {}_tv_\alpha^{n+1} = ({}_tv_{j\alpha}^{n+1})({}_tw_j). \quad (98)$$

Further, chapter 4.4.3 mentions \mathbf{q} can be chosen arbitrarily. The Galerkin discretization of a d -dimensional space with m grid nodes therefore uses the standard basis functions $e_1, e_2, \dots, e_{d \times m}$. Due to the scalar-product $d \times m$ equations would need to be solved:

$$\frac{1}{\Delta t} \int_{\Omega^{t^n}} ({}_tw_i)({}_t\rho)({}_tw_j)({}_tv_{j\alpha}^{n+1} - {}_tv_{j\alpha}^n)d_t\mathbf{x} = - \int_{\Omega^{t^n}} \frac{\partial {}_tw_i}{\partial {}_tx_\beta}\sigma_{\alpha\beta}d_t\mathbf{x}. \quad (99)$$

A mass matrix can be factored out as:

$$m_{ij}^n = \int_{\Omega^{t^n}} {}_t w_i({}_t \rho) {}_t w_j d_t \mathbf{x}. \quad (100)$$

The Lagrangian pull-back relates this to the initial density in the Lagrangian view and discretizing the integral with the initial time-invariant particle mass $m_p \approx V_p^0 \rho({}_0 x_p, 0)$:

$$m_{ij}^n = \int_{\Omega^{t^0}} ({}_t w_i)({}_0 \rho_0)({}_t w_j) d_0 \mathbf{x} \approx \sum_p m_p w_i(\mathbf{x}_p) w_j(\mathbf{x}_p). \quad (101)$$

This matrix is symmetric positive semi-definite (since mass is positive). Numerically this matrix is mostly not used as is due to possibility of it being singular. This is solved commonly due to a mass-lumping strategy. Replacing m_{ii}^n with the i -th row sum and clearing all other elements leads to a diagonalization

$$\sum_p m_p w_{ip} w_{jp} \stackrel{70}{\approx} \sum_p m_p w_{ip} \stackrel{75}{=} m_i^n, \quad (102)$$

where partition of unity $\sum_j w_{jp} = 1$ is used. This is exactly the mass transfer as in equation 75, s.t. no further assembling of a mass matrix is needed. The discretization of the right side of 99 happens with an estimated per particle stress $\sigma_p^{n+\lambda}$:

$$\int_{\Omega^{t^n}} \frac{\partial_t w_i}{\partial_t x_\beta} \sigma_{\alpha\beta} d\mathbf{x} \approx \sum_p (\sigma_p^{n+\lambda})_{\alpha\beta} \frac{\partial w_{ip}^n}{\partial x_\beta} V_p^n. \quad (103)$$

Setting in equation 102 and 103 into 99 summarizes the space discretization as:

$$\frac{1}{\Delta t} ((m^n \mathbf{v}^{n+1})_i - (m^n \mathbf{v}^n)_i) = - \sum_p \sigma_p^{n+\lambda} \nabla w_{ip}^n V_p^n = \mathbf{f}_i^{n+\lambda}. \quad (104)$$

The momentum change of the left side is by construction equal to a (grid node) force.

Given, that the material point method keeps track of the deformation by a deformation gradient, each particle will have one associated with it for the deformation of its local neighborhood \mathbf{F}_p^n . Based on this one may also gain a volume change measure around the particle as $J_p^n = \det(\mathbf{F}_p^n)$. Starting with an initial volume of a particle V_p^0 the volume may be tracked in time by:

$$V_p^n \stackrel{24}{\approx} V_p^0 J_p^n. \quad (105)$$

In equation 57 an alternate measure for the stress by the first Piola-Kirchhoff stress is given. The results of 104 may therefore equally expressed by it:

$$\begin{aligned} \mathbf{f}_i^{n+\lambda} &\stackrel{57,105}{=} - \sum_p \frac{1}{J_p^n} \mathbf{P}_p^{n+\lambda} (\mathbf{F}_p^n)^T \nabla w_{ip} V_p^0 J_p^n \\ &= - \sum_p \mathbf{P}_p^{n+\lambda} (\mathbf{F}_p^n)^T \nabla w_{ip} V_p^0. \end{aligned} \quad (106)$$

[Jia+16] [JST17] [Bat06]

4.6.3 Deformation gradient evolution

In equation 50 the evolution of the deformation gradient is shown to be:

$$\frac{\partial_0^t \mathbf{F}}{\partial t} = \nabla_0 \mathbf{v}({}_0\mathbf{x}, t). \quad (107)$$

Discretizing the Lagrangian deformation gradient in time with equation 95 results in:

$$\frac{\mathbf{F}_p^{n+1} + \mathbf{F}_p^n}{\Delta t} = \nabla_0 \mathbf{v}^{n+\lambda}({}_0\mathbf{x}). \quad (108)$$

Pushing the right side forward to Eulerian view

$$\frac{\mathbf{F}_p^{n+1} + \mathbf{F}_p^n}{\Delta t} = \nabla_t \mathbf{v}^{n+\lambda}({}_t\mathbf{x})_0^t \mathbf{F} = \nabla_t \mathbf{v}^{n+\lambda}({}_t\mathbf{x}) \mathbf{F}_p^n \quad (109)$$

and further applying the Galerkin discretization

$$({}_t\mathbf{v}^{n+\lambda})_\alpha = (v_i^{n+\lambda})_\alpha w_i \Rightarrow \frac{\partial({}_t\mathbf{v}^{n+\lambda})_\alpha}{\partial x_\beta} = (v_i^{n+\lambda})_\alpha \frac{\partial w_i}{\partial x_\beta} \quad (110)$$

leads to the final update rule for the deformation gradient:

$$\mathbf{F}_p^{n+1} = \left(\mathbf{I} + \Delta t \sum_i \mathbf{v}_i^{n+\lambda} (\nabla w_{ip})^T \right) \mathbf{F}_p^n. \quad (111)$$

The discretization of the position will also be necessary to advance the particles and weight them back:

$$\frac{\partial_t \mathbf{x}}{\partial t} = {}_t\mathbf{v} \Rightarrow \frac{\hat{\mathbf{x}}_i^{n+1} - \mathbf{x}_i^n}{\Delta t} = \mathbf{v}_i^{n+\lambda}. \quad (112)$$

The grid position $\hat{\mathbf{x}}_i^{n+1}$ does not correspond to an actual deformation. The grid never actually gets deformed (unlike in FEM-methods). The discretized evolution of the deformation gradient 111 is directly a function of $\hat{\mathbf{x}}$. For the point $\hat{\mathbf{x}}_i^{n+1}$ this becomes:

$$\hat{\mathbf{F}}_p^{n+1}(\hat{\mathbf{x}}_i^{n+1}) = \left(\mathbf{I} + \sum_i (\hat{\mathbf{x}}_i^{n+1} - \mathbf{x}_i^n) (\nabla w_{ip})^T \right) \mathbf{F}_p^n. \quad (113)$$

As part of the class of time integrators in use (95) a function of \mathbf{x}_i gets evaluated at an in-between point given by:

$$\mathbf{x}_i^{n+\lambda} = \lambda \mathbf{x}_i^{n+1} + (1 - \lambda) \mathbf{x}_i^n. \quad (114)$$

Plugging this point into 113 leads to the following generalization:

$$\begin{aligned} \hat{\mathbf{F}}_p^{n+\lambda}(\mathbf{x}_i^{n+\lambda}) &= \left(\mathbf{I} + \lambda \sum_i (\hat{\mathbf{x}}_i^{n+1} - \mathbf{x}_i^n) (\nabla w_{ip})^T \right) \mathbf{F}_p^n \\ &= (1 - \lambda) \mathbf{F}_p^n + \lambda \hat{\mathbf{F}}_p^{n+1}. \end{aligned} \quad (115)$$

[Jia+16]

4.6.4 Grid nodal forces

The notion of a total elastic potential energy function Ψ was introduced in chapter 4.3.2. The MPM approximation to this function can be defined by:

$$e(\hat{\mathbf{x}}) = \sum_p V_p^0 \Psi(\hat{\mathbf{F}}_{Ep}(\hat{\mathbf{x}})). \quad (116)$$

The evolution of the deformation gradient 113 for a general $\hat{\mathbf{x}}_i$ is necessary

$$\frac{\partial \hat{F}_{\omega\beta}}{\partial \hat{x}_\alpha} = \delta_{\omega\alpha} \frac{\partial w_{ip}}{\partial x_\gamma} F_{\gamma\beta} = \delta_{\omega\alpha} F_{\gamma\beta} \frac{\partial w_{ip}}{\partial x_\gamma} \quad (117)$$

for the spatial derivative of the potential $e(\hat{\mathbf{x}})$. This is just the force created by elastic stresses out of equation 106:

$$\begin{aligned} \frac{\partial e}{\partial \hat{x}_{i\alpha}}(\hat{\mathbf{x}}) &= \sum_p V_p^0 \frac{\partial \Psi}{\partial \hat{F}_{\omega\beta}}(\hat{\mathbf{F}}_{Ep}) \frac{\partial \hat{F}_{\omega\beta}}{\partial \hat{x}_\alpha} \\ &= \sum_p V_p^0 P_{\alpha\beta}(\hat{\mathbf{F}}_{Ep}) F_{\gamma\beta} \frac{\partial w_{ip}}{\partial x_\gamma} = -\hat{f}_{i\alpha}. \end{aligned} \quad (118)$$

The nodal force can be also described in terms of the Cauchy stress:

$$\hat{\mathbf{f}}_i = - \sum_p V_p^n \boldsymbol{\sigma}_p(\hat{\mathbf{F}}_{Ep}) \nabla w_{ip}^n. \quad (119)$$

Due to equation 115 the stress computation is summarized for the class of functions in use as:

$$\mathbf{P}^{n+\lambda}(\hat{\mathbf{F}}_{Ep}) = \mathbf{P}(\hat{\mathbf{F}}_{Ep}^{n+\lambda}), \quad \boldsymbol{\sigma}^{n+\lambda}(\hat{\mathbf{F}}_{Ep}) = \boldsymbol{\sigma}(\hat{\mathbf{F}}_{Ep}^{n+\lambda}). \quad (120)$$

[Jia+16][JST17]

4.6.5 Symplectic midpoint scheme

Starting from the last update on the grid which is typically the position with equation 95 the general midpoint scheme ($\lambda = \frac{1}{2}$) is:

$$\hat{\mathbf{x}}_i^{n+1} = \mathbf{x}_i^n + \Delta t \mathbf{v}_i^{n+\frac{1}{2}}. \quad (121)$$

Due to 104 a velocity update can be put together as:

$$\hat{\mathbf{v}}_i^{n+1} = \mathbf{v}_i^n + \frac{\Delta t}{m_i^n} \mathbf{f}_i^{n+\frac{1}{2}}. \quad (122)$$

A variable of $n + \frac{1}{2}$ then gets evaluated at the midpoint (114):

$$\mathbf{f}_i^{n+\frac{1}{2}} = \mathbf{f}_i \left(\frac{\mathbf{x}_i^n + \hat{\mathbf{x}}_i^{n+1}}{2} \right). \quad (123)$$

The modified energy conserving implicit midpoint scheme from [Gon00] for the material point method differs by the use of a trapezoidal approximation of $\mathbf{v}_i^{n+\frac{1}{2}}$:

$$\mathbf{v}_i^{n+\frac{1}{2}} \approx \frac{\hat{\mathbf{v}}_i^{n+1} + \mathbf{v}_i^n}{2}. \quad (124)$$

The trapezoidal rule has the same order of error $O(\Delta t^2)$ as the implicit midpoint scheme. This modification allows for a more direct one-step scheme as shown in the following. Plugging \mathbf{x}_i^{n+1} of equation 121 into 122 leads to the discretized momentum equation:

$$\mathbf{h}(\hat{\mathbf{v}}_i^{n+1}) = m_i^n \frac{\hat{\mathbf{v}}_i^{n+1} - \mathbf{v}_i^n}{\Delta t} - \mathbf{f}_i \left(\mathbf{x}_i^n + \frac{\Delta t}{4} (\hat{\mathbf{v}}_i^{n+1} + \mathbf{v}_i^n) \right) = 0. \quad (125)$$

One can recast this method back to an energy function by integrating

$$E(\mathbf{v}_i) = \sum_i \frac{m_i^n}{8} \|\mathbf{v}_i - \mathbf{v}_i^n\|_2^2 + e(\mathbf{x}_i^n + \frac{\Delta t}{4} (\mathbf{v}_i + \mathbf{v}_i^n)) \quad (126)$$

where e is just the discretized elastic potential energy out of 116. In general this is an optimization objective that needs minimizing to solve for the updated velocities. Recasting allows to solve the energy objective in a general manner by an optimization integrator.

In general starting off with an energy description is a more physical approach of the problem. The first term can be identified clearly as the kinetic energy. Moreover, it easily allows adding potential terms for gravity or collisions [Gas+15], or modifying the energy function altogether based off for instance the fundamental state of matter: as an example the phase transition to and physics of a liquid [Sto+14]. The analysis of minimizing the objective is equivalent to finding the zero crossing of the derivative:

$$\operatorname{argmin}_{\forall \mathbf{v}_i} (E(\mathbf{v}_i)) \Leftrightarrow g(\mathbf{v}_i) = \frac{\partial E}{\partial \mathbf{v}_i} = 0. \quad (127)$$

Since the objective is minimizing, the scale of \mathbf{E} can be chosen arbitrarily. I.e. a zero crossing does not scale. The scaling here can be identified as:

$$\mathbf{g}(\mathbf{v}_i) = \frac{\Delta t}{4} h(\mathbf{v}_i) = m_i^n \frac{\mathbf{v}_i - \mathbf{v}_i^n}{4} - \frac{\Delta t}{4} \mathbf{f}_i \left(\mathbf{x}_i^n + \frac{\Delta t}{4} (\mathbf{v}_i + \mathbf{v}_i^n) \right). \quad (128)$$

[Jia+16][JST17]

4.6.6 Newton's Method

Many minimization and root finding algorithms are available. One of such is Newton's Method, which allows for rapid quadratic convergence in a near local neighborhood.

$$\mathbf{v}_i^{(i+1)} = \mathbf{v}_i^{(i)} + \left[\frac{\partial \mathbf{g}}{\partial \mathbf{v}} \left(\mathbf{v}_i^{(i)} \right) \right]^{-1} \mathbf{g} \left(\mathbf{v}_i^{(i)} \right) \quad (129)$$

Algorithm 1 Conjugate gradient

```

1: procedure CONJUGATE-GRADIENT( $H, x, f$ )
2:    $\mathbf{x} \leftarrow \text{INITIALGUESS}()$ 
3:    $\mathbf{Hx} \leftarrow \text{COMPUTEHP}(x)$ 
4:    $\mathbf{r} \leftarrow \mathbf{f} - \mathbf{Hx}$ 
5:    $\mathbf{p} \leftarrow \mathbf{r}$ 
6:    $\gamma \leftarrow \langle \mathbf{r}, \mathbf{r} \rangle$ 
7:   repeat
8:      $\mathbf{Hp} \leftarrow \text{COMPUTEHP}(p)$ 
9:      $\mathbf{s} \leftarrow \mathbf{Hp}$ 
10:     $\alpha \leftarrow \frac{\gamma}{\langle \mathbf{p}, \mathbf{s} \rangle}$ 
11:     $\mathbf{x} \leftarrow \mathbf{x} + \alpha \mathbf{p}$ 
12:     $\mathbf{r} \leftarrow \mathbf{r} - \alpha \mathbf{s}$ 
13:     $\kappa \leftarrow \langle \mathbf{r}, \mathbf{r} \rangle$ 
14:    if  $\kappa < \epsilon$  then ▷ alt. fixed amount of steps
15:      return
16:    end if
17:     $\beta \leftarrow \frac{\kappa}{\gamma}$ 
18:     $\mathbf{p} \leftarrow \mathbf{r} + \beta \mathbf{p}$ 
19:     $\gamma \leftarrow \kappa$ 
20:  until false ▷ exit at 15
21: end procedure

```

Computing the inverse is numerically irresponsible. Instead the following linear system is solved ($\Delta \mathbf{v} = \mathbf{v}_i^{(i+1)} - \mathbf{v}_i^{(i)}$):

$$\left[\frac{\partial \mathbf{g}}{\partial \mathbf{v}} \left(\mathbf{v}_i^{(i)} \right) \right] \Delta \mathbf{v} = \mathbf{g} \left(\mathbf{v}_i^{(i)} \right). \quad (130)$$

Using the Newton's Method however requires a computation of the Hessian of $E(\mathbf{v}_i)$:

$$\frac{\partial \mathbf{g}_i}{\partial \mathbf{v}_j} = \frac{m_i^n}{4} - \frac{\Delta t^2}{16} \frac{\partial \mathbf{f}_i}{\partial \mathbf{x}_j} \left(\mathbf{x}_i^n + \frac{\Delta t}{4} (\mathbf{v}_i + \mathbf{v}_i^n) \right). \quad (131)$$

Computing $\frac{\partial \mathbf{f}_i}{\partial \mathbf{x}_j}$ for every combination ij would be quite memory-intensive. Instead immediately the matrix-vector product on an increment $\delta \mathbf{u}_j$ is solved:

$$\sum_j \frac{\partial \mathbf{g}_i}{\partial \mathbf{v}_j} \delta \mathbf{u}_j = \frac{m_i^n}{4} \delta \mathbf{u}_j - \frac{\Delta t^2}{16} \sum_j \frac{\partial \mathbf{f}_i}{\partial \mathbf{x}_j} \left(\mathbf{x}_i^n + \frac{\Delta t}{4} (\mathbf{v}_i + \mathbf{v}_i^n) \right) \delta \mathbf{u}_j. \quad (132)$$

$\frac{\partial \mathbf{g}}{\partial \mathbf{v}}$ is symmetric, positive definite due it being the Hessian of a convex energy function E of a hyper-elastic material. The linear system of equations 130 can be solved with the conjugate gradient method (Algorithm 1). There is two important things to notice:

1. One may want to use a preconditioner P^{-1} to reduce iteration times. However, conservation of momentum on incomplete convergence is fulfilled if 130 is premultiplied by the inverse diagonal mass matrix M^{-1} [JST17]. Thus the equation becomes:

$$\begin{aligned} & \left(\frac{1}{4} - \frac{\Delta t^2}{16} \frac{1}{m_i^n} \frac{\partial \mathbf{f}_i}{\partial \mathbf{x}_j} \left(\mathbf{x}_i^n + \frac{\Delta t}{4} (\mathbf{v}_i^{(i)} + \mathbf{v}_i^n) \right) \right) \Delta \mathbf{v} \\ &= \frac{\mathbf{v}_i^{(i)} - \mathbf{v}_i^n}{4} - \frac{\Delta t}{4} \frac{1}{m_i^n} \mathbf{f}_i \left(\mathbf{x}_i^n + \frac{\Delta t}{4} (\mathbf{v}_i^{(i)} + \mathbf{v}_i^n) \right). \end{aligned} \quad (133)$$

2. Due to 132 the product of the Hessian with an increment $(\sum_j \frac{\partial \mathbf{f}_i}{\partial \mathbf{x}_j} \delta \mathbf{u}_j)$ needs to be computed anew every step since a pure matrix store is too costly.

The Hessian is derived following 117 and 118:

$$\frac{\partial e}{\partial x_{i\alpha} \partial x_{j\tau}} = \sum_p V_p^0 \frac{\partial^2 \Psi}{\partial F_{\alpha\beta} \partial F_{\tau\sigma}} (F_p^n)_{\omega\sigma} \frac{\partial w_{jp}}{\partial x_\omega} (F_p^n)_{\gamma\beta} \frac{\partial w_{ip}}{\partial x_\gamma} = - \frac{\partial f_{i\alpha}}{\partial x_{j\tau}}. \quad (134)$$

The Hessian increment can be computed with a two-stage process:

1. Compute a particle quantity \mathbf{A}_p with a grid-to-particle-transfer:

$$\mathbf{A}_p = \frac{\partial^2 \Psi}{\partial \mathbf{F} \partial \mathbf{F}} (\hat{\mathbf{F}}_p(\hat{\mathbf{x}})) : \left(\sum_j \delta \mathbf{u}_j (\nabla w_{jp}^n)^T \mathbf{F}_p^n \right). \quad (135)$$

2. Compute the Hessian increment $(\delta \mathbf{f}_i)$ with a particle-to-grid-transfer:

$$- \delta \mathbf{f}_i = - \sum_j \frac{\partial \mathbf{f}_i}{\partial \mathbf{x}_j} \delta \mathbf{u}_j = \sum_p V_p^0 \mathbf{A}_p (\mathbf{F}_p^n)^T \nabla w_{ip}^n. \quad (136)$$

Memory	Location on/off chip	Cached	Scope	Lifetime
Register	On	n/a	1 thread(no shuffle)	thread
Local	Off	L2	1 thread	thread
Shared	On	n/a	block	block
Global	Off	L2	all threads+host	host alloc

Table 1: GPU Memory [NVIb]

4.7 General-purpose computing on graphics processing units

This chapter is split into two parts. 4.7.1 tends to the memory hierarchy of the GPU and typical optimizations done in GPGPU work. Furthermore, chapter 4.7.2 will elaborate metrics to quantify optimizations.

4.7.1 GPGPU Optimization opportunities

The speed of these memory types is given in the following starting with the fastest: Register > Shared Memory > Local, Global. Table 1 gives an overview over their capabilities which is referred to in the following.

Therefore, one should prefer register memory for intra-thread caching. Shared-memory should be used for extra caching memory(to reduce register spilling) or inter-thread communication within a block. Global memory is the persistent storage on the GPU.

Host communication: A common performance bottleneck is stalling the GPU with CPU-GPU transfers. The attainable bandwidth for PCIe x16 3.0 between host and device is 16GB/s while the communication between device and GPU is 224GB/s (GTX 970) [NVId]. This includes doing calculations on the GPU that may run faster on the CPU. The API may also stall the GPU if the CPU is not issuing instructions fast enough to the GPU. This may be due to calculations on the CPU or, even worse, calculations depending on GPU results. This thesis tries to avoid PCI-transfers wherever possible.

Memory coalescing: Between a single thread and a block of threads another important entity exists. NVIDIA GPUs group 32 threads into a synchronous warp, respectively AMD groups 64 threads as a wavefront. In general they are called subgroups. All operations are issued per subgroup. A memory access uses the L2-caching behavior. A L2-cache-line is 32 bytes long. Thus eight (u)int/floats, two single-precision vectors or a single double-precision vector fit into one cache-line. If all threads of a warp access memory within this cache-line, only one memory request of 32 bytes needs to be made. In contrast, if a warp accesses N different cache-lines, N*32 bytes need to be loaded.

The unified L1/texture-cache acts as a coalescing buffer for the thread of a subgroup (Maxwell architecture [NVIe]). It does not matter in which order the cache-line is accessed by the warp. I.e. random or reversed access on a single cache-line are also coalesced. On a global level the easiest to control access pattern

thus becomes consecutive or reversed memory accesses. L2 is a write back cache. Thus this assessment also qualifies for global memory writes. [Sch]

Shared Memory bank conflicts: Shared memory is split into 32 banks of 4 bytes. The hardware groups together unique memory accesses on these banks. E.g., if two threads within a subgroup access bank 17, a bank conflict occurs, and the access needs to be split into two groups. The one exception is a broadcast: All threads within a subgroup access the same bank. The number of banks is equal to the warp size on the GTX970 s.t. throughput for 32 floats is maximized if every thread does a unique bank access. [NVIf]

Register spilling: Local memory should be avoided. Local memory is created due to register spilling and stored off chip like global memory, though it is L2-cached. The available number of registers per thread is calculable with the CUDA Occupancy Calculator [NVIf] on NVIDIA hardware. If the occupancy falls off to 0%, register spilling occurs. The occupancy is either given absolute due the amount of active warp or relative divided by the possible maximum amount of warps on a Streaming Multiprocessor(SM). Occupancy allows the SM to schedule between warps: If the current warp cannot continue (memory latency, barrier etc.), the warp scheduler will switch to another. This is called a warp stall, table 2. Occupancy is mostly affected due to resource limits on the SM (shared memory, register), as can be seen in the Occupancy Calculator. Non optimal occupancy might not have any performance impact at all when the GPU has enough warps to switch to at all times. [NVIf]

There is no exact way to find out the exact number of registers for any OpenGL shader. The program object assembly output of *nvemulate* [NVIf] may give an indicator. It will output an intermediate language of one of the families of *NV_gpu_programX* (where *X* stands for the version). TEMP variables are registers. Since *NV_gpu_programX* is a family of intermediate languages, there is however no guarantee these are not further optimized. Otherwise, close monitoring of the occupancy is recommended. All other metrics discussed are readily available for OpenGL.

Block size: In general the block size should be chosen as small as possible to not hit resource limits. One should start however with a block size of at least 64, as can be seen in the Occupancy Calculator. Increasing the block size is useful in combination with shared memory usage. Shared memory accesses are instruction-spically faster than global memory accesses. The more threads of a block reuse shared memory data, the faster the memory throughput will be. Therefore, operators which involve filtering (also MPM-transfers) can use this behavior.

Multiple elements per thread: Merging threads and simultaneously reducing block size can reduce register pressure if the algorithm allows it. Otherwise, merging sequential and parallel work improves I/O latency hiding. Since the block size is limited by the GPU, some algorithms need to be split in tree structures to be processed. An indirection cannot be avoided for writing back and loading again from global memory. Therefore, algorithms often improve much further from more sequential work to avoid this indirection.

Loop unrolling: Foremost, loop unrolling reduces instructions and can thus speed up compute-bound work. Moreover, loop unrolling might help the compiler reorder instructions and thus execute instructions faster. Instructions benefiting greatly from this are global loads. [Bav] shows at the example of motion blur and ray-marching that this greatly can increase throughput. Whereas the motion blur example uses a fixed amount of samples and therefore is easily unrollable, ray-marching is a dynamic process. Dynamic loops can however be partially unrolled. In the case of ray-marching this would for instance fetch two samples at once although it might process only one. In short, this merges two consecutive loop iterations. The latency of the second instruction might be partly hidden by the first one and thus speed up the work load. Mind however, that loop unrolling can increase register pressure. More registers need to be stored and process the relevant code where a dynamic loop reuses the same registers for any iteration.

[Aal][NV1b][Bav]

4.7.2 GPU Metrics

The GPU metric topping all others is the raw computing time spend on a shader: Δt_c . The following factors matter to set Δt_c into perspective:

1. For the GPU most interesting is the scalability with increasing input data sizes. All algorithms here however scale linear with the input size.
2. Numerical algorithms may spend additional time computing (implicit) quantities to allow for larger physical time steps: Δt_p . Therefore, one might be interested how long the GPU needs to calculate one physical second:

$$\Delta t_{1s}^c = \frac{\Delta t_c}{\Delta t_p}. \quad (137)$$

Otherwise, one would calculate the speedup of one procedure over a another procedure for a direct comparison:

$$\text{Speedup of Procedure 1} = \frac{\Delta t_{c1}}{\Delta t_{p1}} \frac{\Delta t_{p2}}{\Delta t_{c2}}. \quad (138)$$

The other GPU metrics in table 2 are acquired using NVIDIA Nsight with OpenGL Performance Markers [NVIg].

None of these metrics necessarily have a correlation to computing time. They are however good indicators on which operations/hardware units the GPU spends its time on. The top speed of light(SOL)% metric measures fraction of the throughput to the bandwidth of that hardware unit. NVIDIA aims to get the top SOL% metric between 60% and 80%. Occupancy was discussed in 4.7.1. [Bav]

Aiming to get shaders memory-bandwidth limited, and minimizing the amount of needed accesses for any given workload, is the top priority for simple tasks.

Metric	Max(GTX 970)	Description
Speedup	-	item 2
Δt_c	-	computing time
VRAM SOL%	100	memory throughput w.r.t. to hw.-limit
SM SOL%	100	instruction throughput
L2 SOL%	100	L2-cache throughput
Tex SOL%	100	L1-cache throughput
L2-Hitrate%	100	L2 hit-miss ratio
SM Active%	100	one warp active avg. over SMs
SM Issue Util.%	100	amount of cycles an instr. was issued
SM Occupancy	64.0	active warps avg. over SMs
Read Active%	100	% of time spend on VRAM reads
Write Active%	100	% of time spend on VRAM writes
Warp Stall Reasons:		
Long Scoreboard%	100	VRAM latency (mostly reads)
Short Scoreboard%	100	L2/Shared Mem. latency
Barrier%	100	block synchronization
No Instruction%	100	instruction fetching or waiting on instruction cache miss

Table 2: GPU Performance Metrics

Achieving memory-bandwidth limit is equal to bringing the VRAM SOL% between 60% and 80%. The metrics Read Active%, Write Active% and Long Scoreboard% will simultaneously increase by following that aim.

The metric SM Issue Utilization (per active cycle) is important for compute-bound work, as memory-bandwidth limited work will spend most of its time outside of the SM fetching or writing data. This metric tells if the SM can issue instructions fast. NVIDIA also aims between 60% to 80% for this metric if the shader is compute-bound. Furthermore, for compute-bound work often the top warp stall reason is waiting on instruction fetches.

5 Implementation

The computing time Δt_c of shaders is gained by OpenGL timer queries [Pie14]. A small benchmarker takes care of queuing timer queries and resolving them a frame later. This is done to not stall the GPU pipeline waiting on those queries. At the end of testing data is gathered and statistical quantities are written into a log file.

5.1 GPU memory layout

Listing 2: AoS-Layout

```
struct Particle {  
    vec4 position;  
    vec4 velocity;  
} Particles[n];
```

Listing 3: SoA-Layout

```
struct Container{  
    vec4 positions[n];  
    vec4 velocities[n];  
} Particles;
```

Coalescing leads to the motivation of using structure of arrays(SoA) over arrays of structures(AoS) memory layouts. The latter is the more commonly taught approach while high performance CPU code may also prefer SoA. This opens up the field of data-oriented design which is too big to cover and not main part of this thesis.

In short, one might not access every variable of a particle in a shader. I.e. in most compute work one has a pipeline of different passes each requiring another subset of the variables. Assume for instance, one shader only requires the position. Then it is more favorable for consecutive threads to load consecutive position vectors. The cache-line is then filled with position vectors which all will get used. In contrast, in an AoS layout the cache-line will have a position and a velocity loaded but the shader never uses the velocity. This halves the throughput. This process is shown in Figure 1 and 2.

Due to this we motivate the C++-library *magic_get* [Pol] for basic reflection. Our code manipulates AoS layouts into SoA layouts and back using reflection. The MSVC-Compiler has a hard coded stack limit for these kind of operations. A struct may be not bigger than 256 Bytes before throwing a compiler error. With the optional use of double-precision this limit is quite restrictive towards that compiler.

Furthermore, for sizes starting with 256 KB the NVIDIA-Compiler could not link the OpenGL program using the SoA-Layout as in Listing 3. As an alternative meta information is provided in the style of reflection macros. Therefore,

Listing 4: OpenGL Layout

```
// if SoA  
#define Particle PREC_VEC_TYPE  
#define Particle_position 0  
#define Particle_velocity 1  
#define Particle_size 2  
// if AoS  
struct Particle{  
    PREC_VEC_TYPE position;  
    PREC_VEC_TYPE velocity;  
};  
buffer Container{  
    Particle variables [ ];  
};
```

the container is collapsed as in Listing 4. Memory is then accessible by SoA by memory offset and by AoS by variable or by memory offset for a more abstract view of the memory. The AoS setup is shared between C++ and OpenGL code. One could also build a shader using the abstract layout to convert from SoA to AoS. For more coherency converting the whole process to reflection macros is sensible.

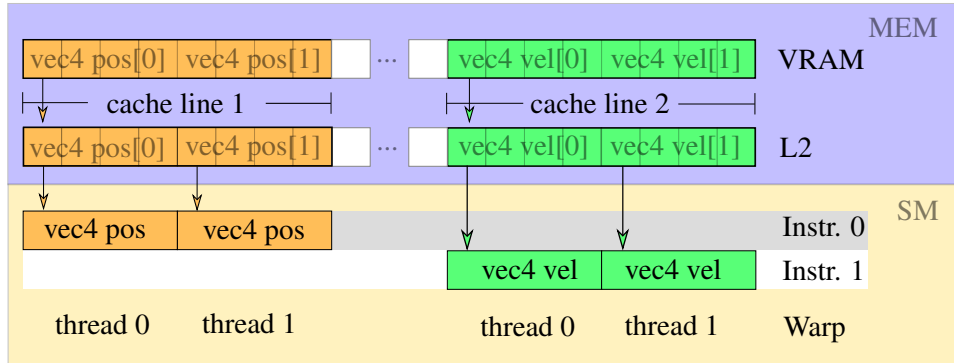


Figure 1: SoA-Layout in practice. The first instruction is shown in orange, the second instruction in green. If green is left out throughput is still maximized

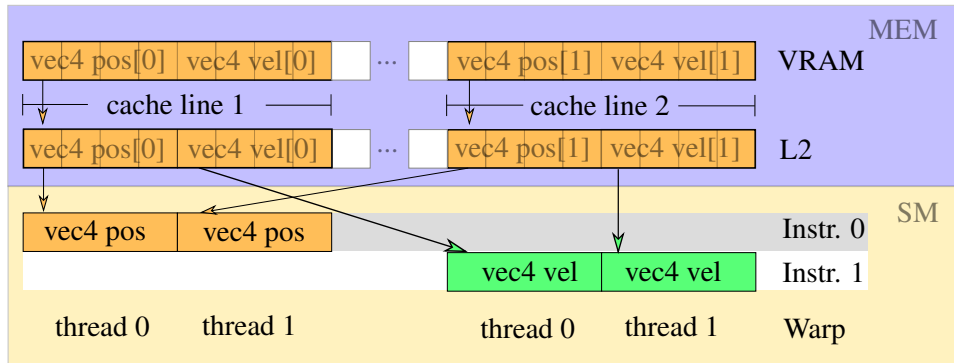


Figure 2: AoS-Layout in practice. The first instruction is shown in orange, the second instruction in green. Orange already loads both cache-lines. If green is left out throughput is halved. Also green is an L2-cache lookup requiring additional overhead over the direct SoA way.

To name a few more cases that macros handle for us:

1. Multiple buffering, e.g. double buffer for unsorted and sorted particles.
2. Single and double precision (PREC_VEC_TYPE in Listing 4).
3. A decorator pattern allows to add buffer information to existing buffer information: For instance index sort needs an extra buffer containing the indices. Full sort requires a double buffer. Thus a sorted buffer gets an attach-

ment(decoration) to contain these information as well as signaling which sort was used in the first place for further operations down the pipeline.

4. Generalize methods to use variants of the same shader with different operations:

```
#define unary_op(x) length(x)
#define binary_op(x,y) x+y
```

For debugging purposes the shader is written to the hard drive with all processed includes. The gcc-preprocessor([Fre]) can preprocess the shader with options: `gcc -E -x c -P`. Except for the omission of the glsl version or extension macros no problems were encountered in this process.

5.2 Parallel Reduction & Scan

The schemes presented in the following are a result of the optimization opportunities discussed in 4.7.1.

Parallel Reduction: Assuming an associative $\text{binary_op}(x, y) := x \circ y$ and an array of values $[a_0, a_1, \dots, a_n]$ reduction computes:

$$r = a_0 \circ a_1 \circ \dots \circ a_n. \quad (139)$$

This OpenGL parallel reduction implementation uses [Har07] as a reference. To avoid memory padding in shared memory the addressing scheme is given by the sequential addressing scheme in Figure 3.

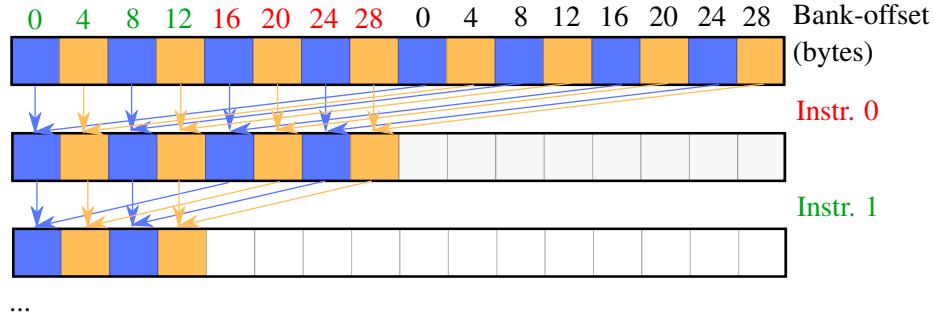


Figure 3: Sequential addressing for `vec4s`. Even threads are blue. Odd threads are yellow. Shared-memory banks per instruction are colored: The banks of the first instruction are green and red numbers. The second instruction is only green. The first and all following instructions can be handled fully concurrently. No memory padding is required.

Parallel reduction schemes using warp shuffle-operations may use sequential or interleaved addressing. Their stride is limited by the memory restrictions imposed due to a warp, Figure 5. [Wes15]

[Har07] also make use of combining parallel and sequential work. Every thread adds a multiple of two sequential adds into shared memory. After this the thread

does its parallel work. Therefore, the reduction factor one invocation does is multiple times higher and allows higher input data sizes without losing any performance, refer to chapter 6.

Parallel reduction solves, assuming a $\text{unary_op}(x)$ directly after memory load, the following problems in MPM:

- CFL condition of chapter 4.5.4 with operators,
 - $\text{unary_op}(x) := \text{length}(x)$ and
 - $\text{binary_op}(x, y) := \max(x, y)$.
- discretized conservation of governing equations between time steps or transfers in chapter 4.5.2 and 4.5.3 with
 - $\text{unary_op}(x) := x$ and
 - $\text{binary_op}(x, y) := x + y$.
- calculate the maximum count of particles of all bins within a block (*per-block parallel reduction* 5.4.3):
 - $\text{unary_op}(x) := x$ and
 - $\text{binary_op}(x, y) := \max(x, y)$.

Scan: Assuming an associative $\text{binary_op}(x, y) := x \circ y$, a neutral element e of the binary_op , and an array of values $[a_0, a_1, \dots, a_n]$ an exclusive scan computes the array:

$$[e, a_0, (a_0 \circ a_1), (a_0 \circ a_1 \circ a_2), \dots, (a_0 \circ a_1 \circ a_2 \circ \dots \circ a_{n-1})]. \quad (140)$$

The scan uses an interleaved addressing pattern, Figure 5. The interleaved addressing pattern has the benefit over the sequential one of already computing the partial scans for all odd indices (although misaligned). Note, that the reduction needs to reduce to the right achieved by writing into the right element instead of the left in Figure 4. A full scan is then computed as [HSO07]:

1. Upsweep-Phase: Top-to-Bottom reduction to the right of the array.
2. Inserting the neutral element into the last element of the array.
3. Downsweep-Phase: Reverse execution order of item 1 (inverted tree), and in addition overwrite the left element with the right one's.

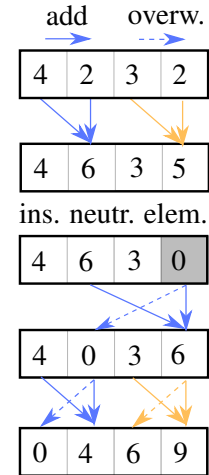


Figure 4: Scan (add)

Again, sequential work can be combined with parallel work. [Bax13] name the process: Raking. The general technique is also called register blocking. Instead of loading one element per thread, one thread loads N elements and computes a sequential partial scan in register memory. The reduced last value of the array is written into shared memory and the parallel scan begins. Afterwards the parallel scan result is spread out(raking) with the sequential partial scan.[Bax13] As

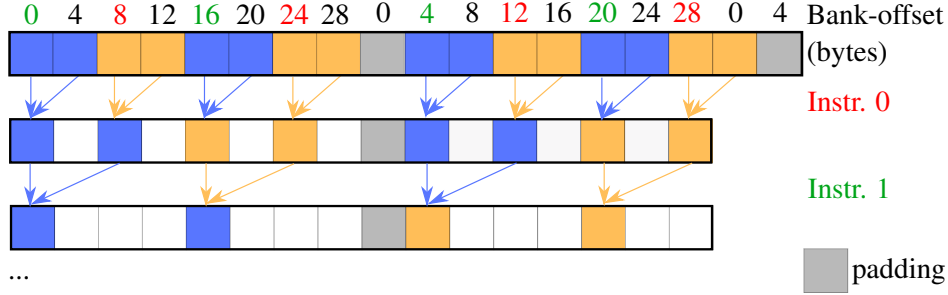


Figure 5: Interleaved addressing `vec4s`. Even threads are blue, odd are yellow. Shared-memory banks per instruction are colored: The banks of the first instruction are colored: The banks of the first instruction are green and red numbers. The second instruction is only green. Memory padding needs to be done for concurrent shared-memory access. The first and all following instructions can be handled fully concurrently.

mentioned, the interleaved addressing requires a memory padding for conflict-free addresses. For block sizes of 32 - 512 this becomes:

$$p = u + (u << \log_2(n)), \text{ or } p = u + \frac{u}{n} \quad (141)$$

where p is the padded memory offset, u is the unpadded memory offset and n is the number of banks. For a block size of 1024 additional padding is needed for a full conflict-free access:

$$p = u + (u << \log_2(n)) + (u << (2 * \log_2(n))), \text{ or } p = u + \frac{u}{n} + \frac{u}{n * n}. \quad (142)$$

However, the added computation time does not outweigh the bank-conflicts. So the process is reverted to equation 141. Note, that this is a correction to [HSO07] where C++-Operator-Precedence of $+$ over $<<$ is not recognized, and additionally incorrectly $u << n$ is used in the first part of equation 142.

A scan is used to calculate memory offsets for stream compaction or sorting algorithms.

One can also calculate a per block scan (with halo) without doing a full scan for every block (Appendices B). This implementation did not end up using this more closely related approach to [Hoe14] as it would commit shared memory bank-conflicts defying the architecture of the GPU. It also puts restriction on the maximum allowed particles per block. Instead preferred is batching a fixed amount of particles, more in chapter 5.4.

The input size for reduction and scan is limited. It's calculable by the *block size* \times *sequential loads*. To support bigger input sizes pyramid structures are in use to process the elements the blocks reduced. In this implementation the input size is mostly reduced s.t. the first level above in the pyramid can be computed within a single block. For the scan this result is then written back. This was enough for the input sizes employed and can be similarly extended by pyramid structures.

5.3 Counting sort & stream compaction

Sorting on the GPU can dramatically increase workload performance of subsequent steps if they can profit from following things:

1. Accesses can now be handled in a coalesced fashion.
2. Data can now be reused due to L2-Cache and/or shared memory.

This is the case for algorithms which require neighbor communication. Supported is a full deep copy of all particle variables. A deep copy profits from item 1 and 2 but takes a hit in performance of uncoalesced accesses for all variables. Alternatively, an indexing to access an existing particle buffer in the specified sorted manner is although supported. Indexing only profits from item 2 and subsequent shaders will be uncoalesced.

Stream compaction reduces applicable data for subsequent operations. The applicable data is checked by a condition. There are a lot of cases where stream compaction can reduce running times: In chapter 2 particle activation is mentioned as one of such. Chapter 5.4.3 will reduce active blocks with an indexed stream compaction. Collision treatment could be implemented as an operation following a collision detection etc. Again indexing and deep copies can be executed for the same reasons mentioned in 1 and 2.

Counting sort: As the sorting algorithm of choice counting sort is used. Counting sort is split into three parts:

1. **Binning:** Transform the particle position into the grid space s.t. every integer in range corresponds to a grid node. Bin due to flooring the transformed particle: Store the particle count c_i of this grid node on the particle as an offset o_p into this grid node.

$$o_p := c_i.$$

Following that, up the counter on the grid by one:

$$c_i := c_i + 1.$$

This process is visualized in Figure 6.

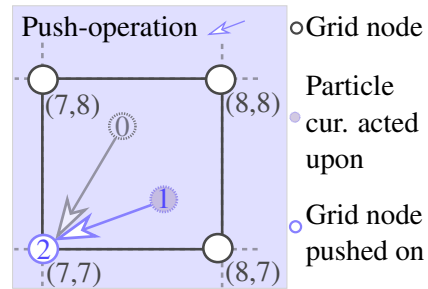


Figure 6: Binning: Particle adds one to c_i after storing it as o_p .

2. **Scan:** Compute a per grid node scan s_i on the counter c_i following 5.2.
3. **Reordering:** $i_p := s_i + o_p$ will now lead to a new ordering of the particle indices. Sorting is now similar to methods `sort_by_key(uint i)` where ordering of particles within the same bin is undefined.

[Hoe14][Klá+17]

The one-dimensional indexing of the grid nodes can be chosen as preferred. Possible are a per-block indexing or a global indexing which are both supported.

Particles could potentially access the same bin at the same time resulting in a race condition. A naive solution to the problem are atomic accesses. As long as the (atomic) writes can be handled coalesced, this process can be done fast by the GPU, chapter 6. This is however only the case for a full deep sort. Therefore, binning in the case of a full sort acts upon the last sorted state. Double buffering particles allows to do so. However, binning is done after a position update that changes the ordering. Full coalescing will therefore generally not occur.

Alternatively, one could work again with the CFL condition. Since particles move at most one bin in the 27-neighborhood, one could mimic a particle-to-grid-transfer, chapter 5.4.2:

1. **Labeling:** Label the particles by the bin they want to change to.
2. **Neighborhood lookup:** A bin then assigns offsets to the particles in the neighborhood and increases its counter.

Similarly to the particle-to-grid-transfer one could choose from the different algorithms presented there to do so. However without additional endeavors the order within a bin is not preserved. One would need to rely on the L1-cache as a coalescing buffer as does the atomic global solution.

Alternatively, one could choose a closer approach to [Hoe14]’s neighborhood search which greedily loads all particles. Ordering can easily be preserved then.

Note that the support in their approach is smaller (27 instead of 64 nodes) and the data required per particle is only the label. Chapter 5.4.3 shows how to do this only for active blocks. Due to the difference in support the same pipeline cannot be used.

In summary, there is little gains to do so yet as binning is only executed once per step and is not the dominant performance cost.

5.4 MPM operations

Easy to parallelize are all operations that are executed entirely on the grid or entirely on the particles:

$$\begin{aligned}\square_p &= \square_p \circ \square_p \circ \dots \circ \square_p, \\ \square_i &= \square_i \circ \square_i \circ \dots \circ \square_i.\end{aligned}$$

One thread will just equal one node or particle, respectively. For one variable assignments a map shader is used that applies a unary operation to any input element. This can be used for instance for the mass divide of momentum on the grid (equation 87) or resetting buffers that are target of global atomic operations.

In contrast much harder are transfers between the two structures that are essential to the material point method:

Particle-to-grid(P2G)-transfers are the mass (equation 75) and momentum (equation 86) transfers to the grid, as well as the computation of the Hessian of equation 136. In general these can be summarized as:

$$\square_i = \sum_p \square_p \circ \square_{ip}.$$

The transfers back to the particles are called grid-to-particle(G2P)-Transfers. Apart from the APIC-transfers (equation 90) and the intermediate Matrix A_p for the Hessian (equation 135), the deformation gradient update F_p^{n+1} is also a G2P-transfer (equation 113). In short, all transfers of the form:

$$\square_p = \sum_i \square_i \circ \square_{ip}.$$

This concludes all necessary operations for the MPM as derived.

The number of transfers per physical time step is much higher than in simple PIC- or SPH-code which are mostly interested in pressure contributions(*float*). This motivates making the transfers a very highly optimized operation. The material point method requires for an elastic material as derived:

1. One P2G-transfer of mass and momentum m_i, v_i (combined *float4*).
2. Per conjugate gradient iteration:
 - (a) One G2P-transfer for the 3×3 Matrix A_p
 - (b) One P2G-transfer of δf_i (*float4*)
3. Per Newton iteration: One G2P-transfer for F_p^{n+1}
4. One G2P-transfer of the 3×3 Matrix B_p^{n+1} , the position x_p^{n+1} and the velocity v_p^{n+1}

In summary, a lot of data is to be transferred between grid and particles which will only increase with more complex models. In contrast, any preprocessing like sorting (chapter 5.3) or filtering active blocks (chapter 5.4.3) need to be executed only once every physical times step. Each transfer can profit from it. Therefore, the transfers are the main focus of this implementation.

The MPM-transfers are different from a typical stencil or filter operation in two main factors:

1. **Dynamic weights:** The stencil is not static. In MPM the weighting function w_{ip} (or ∇w_{ip} etc.) is dependent on the particle position $w_i(\mathbf{x}_p)$. This also means the position needs to be temporarily stored to apply the transfer.
2. **Participating nodes:** A stencil operation reads from a fixed amount of nodes in its neighborhood given by the support of the stencil. This is a node to node relationship which all threads typically participate in from start to finish for the full range of the support.

In a MPM-transfer the number of participating nodes can vary. A node may have one, zero or any positive integer of particles associated with it. Thus in a transfer some nodes may not participate at all or have more load than any of the nodes in its neighborhood.

Item 2 does sound more problematic from a parallelization perspective than it is in practice. In chapter 2 particle resampling is mentioned of a means to fill material gaps. This is an inherent mechanic to control the number of particles within a cell. Although it is designed to augment the numerics, the merge method can be easily used to control the upper boundary of particles within a cell. Nevertheless the number of particles within a cell is still variable. All methods presented in the following are not restricted to bins of a fixed size of particles.

The sorting and binning employed in chapter 5.3 allows to split the grid into a partitioning of blocks. Blocks map well to the thread group nature of GPUs. A single thread within a thread group thus corresponds to a grid node within that block, respectively.

5.4.1 Grid-to-particle transfers

The straightforward solution to this problem is to handle all particles independently from each other. One particle adds up the contributions from each of the grid nodes in range of the interpolation function. In three dimensions this can be done for instance with a two times nested for-loop within a thread. Luckily, grid nodes in a uniform grid are inherently sorted which takes care of coalescing.

Furthermore, sorting particles due to chapter 5.3 increases caching behavior as variables of grid nodes are directly reused by particles in the same group. This results in direct L2-cache hits instead of going the long way of reloading from global memory.

With the mentioned partitioning of the grid into blocks, the shared memory architecture of the GPU can be exploited. This requires two level binning of particles to nodes within blocks [Klá+17]. Figure 7 shows how the G2P-transfer using shared memory is realized. Algorithm 5 shows this process briefly. Due to binning a particle is associated with its lower left node. In Figure 7 four threads are active and form the thread group. All visible grid nodes need to be loaded by the threads. This includes the halo of the block which is dependent upon the support of the interpolation function. For uneven polynomials of the interpolation function the

floored position is very favorable. It allows the left support to be one smaller than the right support. As a result, the weight of a most outer-edge particle (of the active particle region) just reaches zero for any neighborhood-node outside the halo.

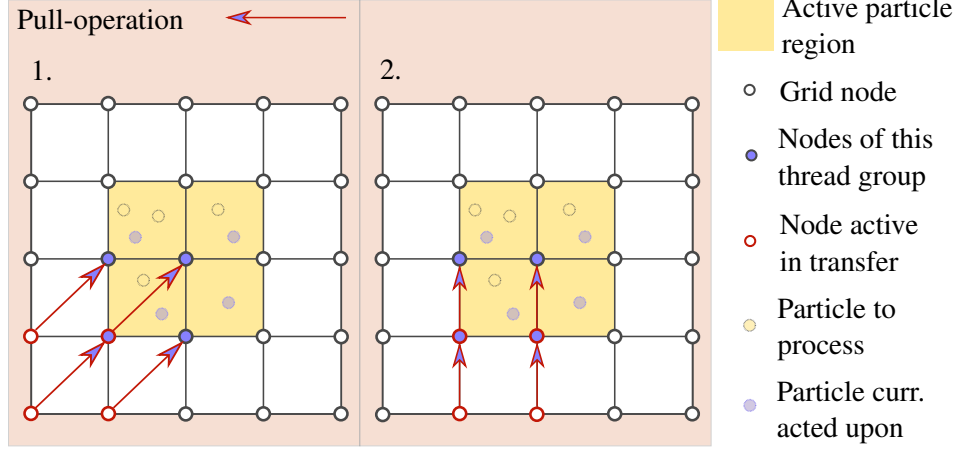


Figure 7: G2P-transfer: The transfer of a single particle is split into 64 sequential runs (using cubic weights). Shown are the first two runs.

The bigger the block the less halo nodes need to be loaded in total. Given an interpolation function with left support l and right support r , total grid size g , and block sizes b_x, b_y, b_z the general function to calculate the number of elements loaded is:

$$m(b_x, b_y, b_z) = \frac{g}{b_x * b_y * b_z} (l + b_x + r)(l + b_y + r)(l + b_z + r). \quad (143)$$

As an example, take a 128*128*128 grid and the cubic interpolation function which has a left support of 1, and a right support of 2. Subdivide the grid into 4*4*4 or 8*4*4 elements respectively:

$$m(4, 4, 4) : 11, 239, 424 \text{ Elements}, m(8, 4, 4) : 8, 830, 976 \text{ Elements}$$

Note however, that in practice there is a good chance, that a majority of the additional elements results in L2-cache hits.

Next up is the transfer: Each thread corresponds to one particle within the blue nodes in Figure 7. The threads run in unison over their relative neighbors within the support and collect the weighted contribution to this particle. In this process the particle's position needs to be loaded to the weighted corresponding contribution. The transfer needs to be repeated for each particle in the bin. Since the number of particles is variable, this loop is dynamic and will lead to branch divergence within a warp. One should rely on external mechanics like particle resampling to reduce branching.

Alternatively, one could come up with a per warp load balancing scheme: One thread would then not directly correspond to one active node. They would need to

Algorithm 5 G2P-transfer

```
1: for all blockNode  $\in$  grid do in parallel
2:   shared vec4 blockAndHalo [H_FLAT]
3:   for all (node, local_id)  $\in$  assignedNodes(blockNode, H_FLAT) do
4:     blockAndHalo[local_id]  $\leftarrow$  node  $\triangleright$  global load
5:   end for
6:   barrier()
7:   for all particle  $\in$  bin(blockNode) do
8:     sum  $\leftarrow$  vec4(.0)
9:     for all neighbor_id  $\in$  support(blockNode) do  $\triangleright$  transfer
10:      wip  $\leftarrow$  weight(particle, neighbor_id)
11:      sum  $\mathrel{+}=$  blockAndHalo[neighbor_id] * wip
12:    end for
13:    particle  $\leftarrow$  sum  $\triangleright$  global write
14:  end for
15: end for
```

act as another node in the same warp when their load is done. This will inevitably lead to shared memory bank conflicts and other difficulties. For the particle push transfers this would necessarily introduce atomic operations on shared memory again.

In Appendices C the accesses of one warp on shared memory banks is shown. The interpolation function is assumed to be cubic and the first block dimension is $x = 4$ or $x = 8$. The shared memory can thus be handled as concurrently as possible.

As an extension to this process batching is introduced. Instead of conservatively loading and writing one particle at a time, each thread handles multiple particles together which it stores in register memory. Important to this process is to unroll the corresponding loops that load, write, as well as process these particles. Instead of needing to rerun the transfer for each particle, the number of runs now is the number of non-batched runs divided by the number of particles. This process adds to the amount of registers allocated and can thus also negatively impact performance.

5.4.2 Particle-to-grid-transfers

Straightforward to implement are various variations on global memory. Consider first binning was not introduced. A grid node would not know how to lookup the particles in its neighborhood. This would require the particle to find and write to the grid node in its support. Since any particle in the neighborhood of a grid node contributes to it, all writes have to be atomic. A typical approach is thus simply parallelizing for each particle and atomically write to the neighbor nodes in a loop. In the unsorted case this stalls the warps immensely. In [Mey15] the static loop

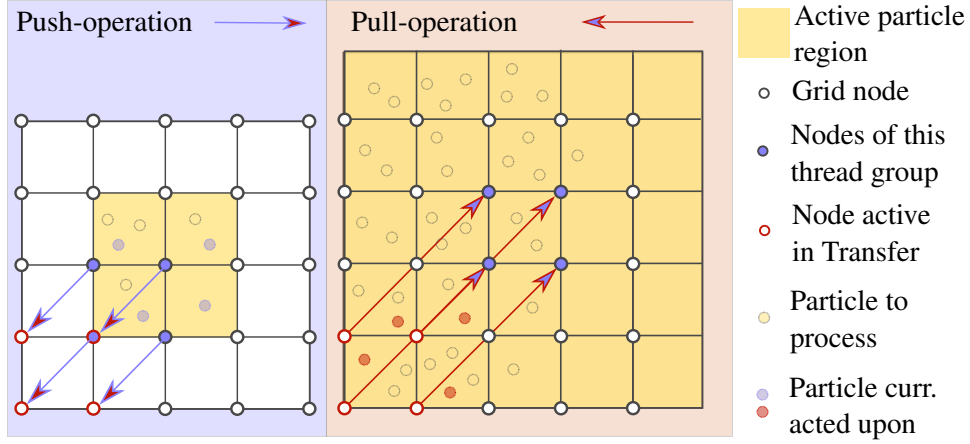


Figure 8: P2G-transfer: The first run is shown. On the left the P2G-sync-transfer is shown that writes into the neighborhood. On the right the P2G-pull approach is shown that instead reads out of the neighborhood.

over the support is also parallelized resulting in higher throughput. The benefits of sorting in chapter 5.3 apply to the P2G-transfers very significantly. The results of above get reversed and looping performs better. Stalling is much less of an issue.

P2G-pull-transfer: Sorting and binning however open up the possibility of shared memory implementations. The equivalent of the G2P-transfer for the P2G-transfer is pulling the relevant data from the neighborhood. The process is shown in Figure 8.

It is important to notice that the supports in the P2G-pull approach are reversed: Left becomes right, right becomes left. Other than that the transfer works in the same way as the G2P-transfer. Instead of reading from grid nodes, reading from particles is done. Consequently, one particle of each bin is loaded into shared memory. This typically puts a lot more strain onto shared memory. For a simple PIC-transfer (equation 77)

$$(m\mathbf{v})_i^n = \sum_p w_i(\mathbf{x}_p) m_p \mathbf{v}_p^n$$

the position \mathbf{x}_p and the velocity \mathbf{v}_p need to be stored in shared memory for every node in the halo. Additionally the count c_i and scan s_i need to be available to load and access particles. For more complex transfers this will get even worse.

By construction the material point method tries to avoid matrices on the grid due to storage cost. Conversely, the particles have matrices defined over them, e.g. $\mathbf{B}_p, \mathbf{F}_p$. In conclusion one should motivate approaches where grid nodes correspond to shared memory due to the shared memory size limitation.

There is one implementation detail left out for the P2G-pull-transfer which is solved in chapter 5.4.3. That is grid nodes do not know if there are any particles in the neighborhood left processing. 5.4.3 solves this by finding the maximum

Algorithm 6 P2G-sync-transfer

```
1: for all blockNode  $\in$  grid do in parallel
2:   shared vec4 blockAndHalo [H_FLAT]
3:   for all local_id  $\in$  assignedNodesID(blockNode, H_FLAT) do
4:     blockAndHalo[local_id]  $\leftarrow$  vec4(.0)
5:   end for
6:   barrier()
7:   for all particle  $\in$  bin(blockNode) do  $\triangleright$  global load
8:     for all neighbor_id  $\in$  support(blockNode) do  $\triangleright$  transfer
9:       wip  $\leftarrow$  weight(particle, neighbor_id)
10:      blockAndHalo[neighbor_id]  $+=$  particle * wip
11:      barrier()  $\triangleright$  uniform flow control needed!
12:    end for
13:  end for
14:  for all (node, local_id)  $\in$  assignedNodes(blockNode, H_FLAT) do
15:    atomicAdd(node, blockAndHalo[local_id])  $\triangleright$  global write
16:  end for
17: end for
```

particle count in the block (with halo). Thus all nodes within the block need to stay active during transfers.

It is possible to delegate this decision down from the block to its subgroups (respecting their respective haloes). Delegating this from the subgroup to the threads is possible as well. Each thread would calculate the summed up count in its neighborhood. But this hardly matters for compute-bound shaders as all other threads need to wait on the thread with the highest count in the subgroup anyway.

In the following the two Particle-Push-Transfers are examined as they put less strain on shared memory:

P2G-atomic-transfer: One can invert the process of pulling into pushing. Instead of reading from shared memory corresponding to particles, this means now writing to shared memory corresponding grid nodes. Accesses now need to be either atomic or explicitly scheduled if blocks are larger than a subgroup.

As can be seen in Figure 5.4.2, push approaches have the big advantage of only needing to load particles within the block region. The transfers then spread the particle's contribution to the grid nodes in the neighborhood. If in algorithm 6 line 11 the `barrier()` is left out, and `atomicAdd()`s on shared memory are in use, this process is straightforward to implement. One has to make sure to reset the shared memory as their contents are otherwise undefined.

The write back to memory however now also needs to feature atomics. This process will be the same in the following synchronized approach. For a node that is part of any halo, `atomicAdd()`s are a strict requirement. Their results are only partially computed and need to be complemented by neighbor blocks. For such a node these are two writes for a side node, four for an edge node, and eight for a

corner node.

P2G-sync-transfer: Warps/Subgroups are inherently synchronized. No race conditions are present between their threads as they all access different memory positions (as can be seen in Figure 8). The problem arises between different warps of the same thread group. In a synchronized approach this is solved by a `barrier()`. Care needs to be taken as the particle loop of line 7 in algorithm 6 is dynamic.

The OpenGL language states the following requirements for external synchronization: "*barrier()* can be called from flow-control, but it can only be called from uniform flow control. (...) In short, (...) every execution must hit the exact same set of *barrier()* calls in the exact same order." [Khr12]

The dynamic loop has to become static within a thread group. The problem is solved in same fashion as in the P2G-pull method with chapter 5.4.3. The maximum particle of each bin within the block without the halo is the minimum amount of times the loop needs to run across the threads to hit uniform flow control.

Warps are still accelerated if all threads within that warp have lower count. They still however have to commit to wait at the same `barrier()`.

In summary all transfers have the same optimal shared-memory access patterns as shown already by Appendices C. Batching is again a valid option that is executed in the same manner by unrolling the corresponding loops. The block size as well as the level of batching can be chosen arbitrarily to optimize for the workload.

5.4.3 Active blocks & maximum block count:

The P2G-pull- and P2G-sync-transfer of chapter 5.4 required the maximum count of particles within a region. The active particle region is the region that needs to get reduced. Therefore, it is sufficient for the P2G-sync-transfer to reduce the counter

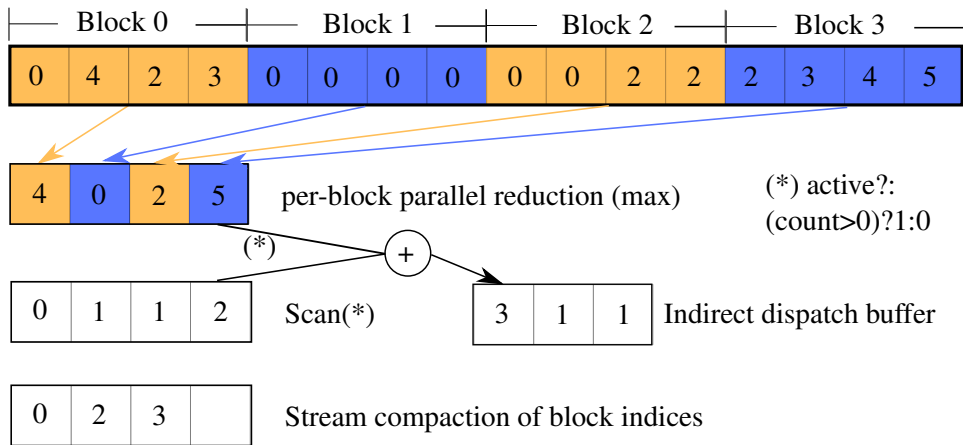


Figure 9: Pipeline to filter active blocks. Returned is the number of active blocks for the launch of a dispatch. A scan and an indexed stream compaction give back the filtered indices to access the active blocks in that dispatch.

within the block, left side of Figure 8. The P2G-pull-transfer however also need to take the halo into account, right side of Figure 8. Both are achievable with a single level of parallel reduction (in contrast to a pyramid). This is the *per block bin count* from now on that uses as the functional input for the parallel reduction:

1. `unary_op(count) = count.`
2. `binary_op(lc,rc) = max(lc,rc).`

For a P2G-sync-transfer one may just start with a parallelization level equal to the blocks employed in 5.4. Then the shader can be narrowed down to do more sequential work to improve throughput. For the P2G-pull-transfer one may also do the first but additionally load all rest elements (by the halo). From there on out more sequential work might be favorable.

If a per block indexing mode is employed, all blocks are directly behind each other in the buffer. Reduction then happens in the typical fashion. A global indexing needs to be permuted such that the indexing puts blocks first.

The process of filtering active blocks can be easily appended. Figure 9 shows the process. An active block is one that has a non-zero per-block counter. The scan that will refer to the active block indices takes thus functional input:

1. `unary_op(count) = (count>0)?1:0`, which uses the ternary operator that increases count by one for any active block.
2. `binary_op(lc,rc) = lc + rc.`

Starting a dispatch for every block only the active blocks will now write their index at the scan's position. It results in an indexed stream compaction. This process is not coalesced. Coalescing will still be guaranteed for all nodes within the block for the P2G-transfers and G2P-transfer. The only uncoalesced access within these shaders is loading the maximum per block count from VRAM which there are few of in comparison.

6 Evaluation

An important part of any operation is to verify them. Chapter 6.1 does that. Following up, chapter 6.2 will use the metrics out of chapter 4.7.2 to evaluate the performance of the implementation.

6.1 Verifying Results

Parallel reduction, map, and scan verify against `std::transform_reduce` as it supplies the same functionality as a fully reduced parallel reduction. It is standard since C++17. These shaders are exact on integers. Floating point precision can be seen in table 3.

Counting sort is tested as a whole by giving back the bin keys of the particles. The bin keys are then tested on the CPU against `std::is_sorted`, which is standard since C++11.

The Eigen-library [JG13] is a well regarded linear algebra library. The **Singular value decomposition** is tested against `Eigen::JacobiSVD`. As a test one million random matrices are created by Eigen. Tests account for the 'Polar SVD'. There is not a single sign error. The average error between the singular values of Eigen and the implementation of chapter 4.2 is 4.91782e-07. $\det(\mathbf{U})$ and $\det(\mathbf{V})$ should be as close as possible to 1. The errors are 3.55707e-07 and 3.26429e-07, respectively.

The **MPM-transfers** need to be mass and momentum conserving. The total mass on the grid m_g^{tot} and the particles m_p^{tot} has to be the same after any transfer:

$$m_p^{tot} = \sum_p m_p = \sum_i m_i = m_g^{tot}. \quad (144)$$

Following this procedure, the same should be true for the total linear momentum \mathbf{p}^{tot} :

$$\mathbf{p}_p^{tot} = \sum_p m_p \mathbf{v}_p = \sum_i m_i \mathbf{v}_i = \mathbf{p}_g^{tot} \quad (145)$$

Shader	unary_op	Total abs. error	Total rel. error
Map (float)	x	0.0	0.0
Map (vec4,dvec4)	length(x)	0.0625	7.94e-08
MapReduce (float)	x	0.0183	3.51e-08
MapReduce (double)	x	1.78e-08	3.42e-14
MapReduce (vec4)	length(x)	212.813	2.71e-04
MapReduce (dvec4)	length(x)	1.58e-05	2.02e-11

Table 3: Error of various shaders on 1024*1024 random elements. Scalars are just between [0.0-1.0]. The vectors have a length between [0.0-1.0].

Quantity	Abs. error	Rel. error
PIC-Transfer		
m_i^{tot}	6.438	6.437e-06
\mathbf{p}_i^{tot}	(0.882,0.977,0.018)	(1.417,1.722,0.003)e-04
\mathbf{L}_i^{tot}	(27.81,43.55,24.35)	(0.024,0.036,0.273)
APIC-Transfer		
m_i^{tot}	7.188	7.188e-06
\mathbf{p}_i^{tot}	(1.230,0.990,0.855)	(1.975,1.745,1.371)e-04
\mathbf{L}_i^{tot}	(0.081,0.184,5.6e-04)	(0.7043,1.510,0.063)e-04

Table 4: Error of 1,000 PIC/APIC-roundtrips of 1M uniformly placed particles with random velocity in a $128 \times 128 \times 128$ grid. Used this instance is a P2G-sync-transfer and G2P-transfer with batching = 4 and block size = (4,4,4). Particles are fixed.

and also for angular momentum \mathbf{L}^{tot} (out of convention upper-case):

$$\mathbf{L}_p^{tot} = \sum_p \mathbf{x}_p \times m_p \mathbf{v}_p = \sum_i \mathbf{x}_i \times m_i \mathbf{v}_i = \mathbf{L}_g^{tot}. \quad (146)$$

The test case spreads one million particles uniformly with random velocities on a $128 \times 128 \times 128$ grid, table 4. A roundtrip consists of a P2G-transfer and a G2P-transfer for relevant variables. In this process the (random) velocities will get filtered. In PIC-transfers this regionally averages out velocities and dissipates angular momentum \mathbf{L}_p . APIC-transfers can conserve the angular momentum better as they define a local velocity field around the particle. Thus table 4 shows the effects on the total error after 1,000 roundtrips.

The total errors vary little between the methods presented in chapter 5.4. They are caused by floating-point inaccuracy. The order of execution on the GPU can vary. Thus the floating-point error will vary from execution to execution.

6.2 Performance

The given metrics in 4.7.2 give valuable insight into how well the GPU can utilize a given shader or program. The GPU was a black box for a long time in this regard. The metrics provided by NVIDIA are a first step to open up the GPUs inner workings. Theory about optimization for the architecture such as [NVib] can be more readily applied. However for abstraction purposes theory as well as descriptions about the architecture might be deliberately vague. These metrics give the programmer more power of identifying the right optimizations for a given code.

All metrics in the following are gathered from a NVIDIA GTX970. All timings are averaged over at least 1000 runs with OpenGL Timer Queries [Pie14]. As more runs are done, the GPU stays very consistent on bringing the average runtime closer to the minimum recorded time. This indicates that the first few runs can take comparably longer.

SoA vs. AoS: In chapter 5.1 is already hinted that throughput could be halved in an AoS-Layout. These effects can be hideous without knowledge of the architecture. Take for instance a map operation (or equivalently a copy operation). Figure 1 and 2 in chapter 5.1 already gave an overview of the procedure for `vec4`. Table 5 compares differences between an AoS- and a SoA-Layout with a buffer of two attributes.

Layout	$\Delta t_c (\mu s)$	Speedup	VRAM	SM	L2	SM Issue Util.
AoS	243	-	77.7%	7.3%	30.3%	6.8%
SoA	120	2.26x	75.4%	14.3%	29.4%	14.0%

Table 5: Metrics between different buffer layouts. Map operation with one instruction
`float x = length(vel)` on 1024×1024 `vec4` buffer storing position and velocity (`vel`).

Immediately apparent becomes that the SoA-Layout is 2.26 times faster. However, both memory subunits(VRAM,L2) have the same utilization as in an AoS-Layout. Though the big difference is in the memory access, the wrong access may be conversely spotted in the non-memory subunits. Since an AoS-Layout loads twice as many `vec4`, every non-memory related metric shrinks by half. An AoS-Layout however issues the same instructions. The SM should do equal work and be active for the same amount of cycles which is not the case.

Layout	$\Delta t_c (\mu s)$	Speedup	VRAM	L2	L2-Hit	Read Active
AoS	275	-	61.3%	41.8%	53.8%	48.9%
SoA	240	1.16x	75.4%	29.4%	20.0%	62.3%

Table 6: Metrics between different buffer layouts. Map operation with two instructions
`float x = length(vel), float y = length(pos)` on 1024×1024 `vec4` buffer storing position(`pos`) and velocity (`vel`).

The case of using both attributes is also visualized in Figure 1 and 2. One map instruction for each attribute is done within the same shader. Table 6 shows the results. Now AoS and SoA load the same amount of elements from VRAM. The SoA-Layout is still faster by $35 \mu s$.

In the SoA-Layout the second attribute lays consecutively in memory and is directly fetched. The SoA timing from table 5 is doubled. As expected the two operations are independent of each other and could thus be separated into two shaders with minimal performance impact; Assuming invocation cost is minimal.

In the AoS-Layout the second attribute lays in the L2-Cache from fetching the first attribute. Thus using the second attribute will yield to cache hits. But going the extra way of checking for the element in the L2-cache requires an additional lookup. Thus in table 6 L2-SOL and L2 Hit rate go up.

The view given was restricted to `vec4` as its the most commonly occurring type. For float/uint data structures the impacts of AoS vs. SoA can be even more

dramatic. Instead of two `vec4`s eight scalars fit into a cache-line. In contrast only one `dvec4` (double-precision) fits into a cache-line. Performance of AoS and SoA in this case is equal.

As a closure the reader is again referred to the subject of data-oriented design. While for non-random access SoA is (as shown) the more efficient layout, random access algorithms can improve performance by using an AoS or mixed setup. In a random access pattern the nearby elements of an SoA-Layout will be left unused in the cache-line.

Parallel Reduction & Scan: Chapter 5.2 presents a shared memory implementation of parallel reduction. To further speed up the work load a sequential pattern is preferred to avoid bank conflicts. Table 7 compares this to an interleaved addressing without padding to illustrate the effects of bank conflicts on performance. Similarly the same can be done for a scan where however the interleaved addressing is preferred anyway. Table 8 shows the comparison for a scan.

Method	Δt_c	Speedup	VRAM	SM	Sel. Warp-Stall Reas.
Interleaved	305	-	23.0%	60.9%	S. Scoreb.(17.2%)
Sequential	141	2.16x	49.8%	37.1%	S. Scoreb.(2.0%)
Seq. (2x)	100	3.05x	69.5%	26.2%	L. Scoreb.(80.1%)
Seq. (128x)	98	3.1x	72.9%	16.9%	L. Scoreb.(84.4%)
Seq. (256x)	101	3.0x	66.4%	14.6%	L. Scoreb.(76.9%)

Table 7: Optimization of one parallel reduction dispatch on 1024×1024 `vec4` with `unary_op(vec4 x)=length(x)` with `block_size = 1024`. Δt_c is in μs . Note that, the interleaved addressing in this example intentionally commits bank conflicts to show performance impacts. The number in parentheses states the number of additional added sequential elements. Reduced is by `block_size` \times sequential elements. Thus they do more work, while also performing better!

The metrics between the parallel reduction and scan differ quite a lot when it comes to the resolve of bank-conflicts. Where the scans issue utilization goes drastically up from 34.2% to 51.3%, the same metric goes down for parallel reduction from 62.2% to 33.0%. SM throughput decreases as VRAM throughput increases although little for the scan. The top warp-stall reason for both is the barrier synchronization between thread groups.

The warp-stall reason however showing the increased throughput due to respecting the shared memory architecture is the Short Scoreboard. The shaders in their original state have no reason to stall for the Short Scoreboard as any memory access is directly fetched. In the parallel reduction case the change is quite visible as this metric drops from 17.2% to only 2.0%.

The second optimization is giving these algorithms more sequential work. This will lighten the SM throughput and increase VRAM throughput as can be seen in both cases. Note, that each thread group in table 7 and 8 does the same amount of parallel work; the sequential work is additionally being done by each thread. However, due to the additional sequential work the amount of thread groups go

Interleaved	Δt_c	Speedup	VRAM	SM	L2	Sel. Stall Reas.
Conflicts	748	-	17.5%	51.7%	8.2%	S. Scoreb.(6.3%)
No confl.	571	1.31x	25.7%	50.1%	5.4%	S. Scoreb.(2.6%)
part. confl.	546	1.36x	23.5%	50.8%	6.0%	S. Scoreb.(3.2%)
Seq. (2x)	323	2.31x	41.7%	43.0%	17.2%	S. Scoreb.(32.0%)
unrolled	258	2.90x	53.8%	42.2%	22.0%	S. Scoreb.(32.0%)
Seq. (4x)	311	2.40x	56.8%	22.7%	37.9%	L. Scoreb.(43.3%)
unrolled	297	2.52x	61.1%	21.2%	40.6%	L. Scoreb.(49.9%)

Table 8: Optimization of one scan dispatch on $4 \times 1024 \times 1024$ integers with `binary_op(x, y) := x+y`. Δt_c in μs , block size is 1024. The number in parentheses states the number of additionally loaded sequential elements. Segment of each scan is `block_size` \times sequential elements. Higher reduction factor corresponds to more work being done.

down by the same factor. As mentioned in [Har07] this saturates I/O-Latency and thus improves performance.

Doing sequential work in parallel reduction adds almost no strain. Thus high amounts sequential work can be done by each thread. The SM work will shrink while the shader get more and more memory-bound. For a reduction factor of 256 first signs of performance decrease can be seen as only four groups are involved in the dispatch. The GTX970 has 13 SMs. Therefore, work is not parallelized enough on a block level anymore. The metric SM active% will go rapidly down at this point. For four groups its 27.8% which is roughly $\frac{4}{13}$.

For the scan this is a little bit harder as elements need to be stored in registers. The effects can be seen in table 8. The segment each scan can handle is by far not as extensive as in parallel reduction. But the speedup achieved from a partially conflict free to an implementation with sequential work, is in contrast much higher. Since each thread requires the nearest by elements, L2-cache hits increase rapidly as does the L2 utilization. Thus the scoreboard stall reasons rise again. Unrolling the static loop which loads the sequential elements additionally hides memory latency.

Counting Sort: The aim of sorting is coalescing as well as increased caching behavior for all following shaders. As a motivation the binning’s similarity to the MPM-Operations might already be highlighted. Table 9 shows how a sorted particle position increases coalescing and L2-Cache hits. The VRAM-throughput increases to 75.3% due to coalescing. Nearby particles hit the same bins and thus L2 rises up to 35.0%. The 6.95x speed up shows how important the sorting as a preprocess is.

Table 10 shows the performance of reordering with index and deep sorting as is. The index sorting will have constant timing across cases. Their writing access will stay uncoalesced. Moreover shaders down the pipeline will also not benefit from coalescing. The binning in table 9 thus for instance always runs on random

Ordering	$\Delta t_c(\mu s)$	Speedup	VRAM	SM	L2	L2-Hit
Random	1,516	-	25.0%	3.4%	9.1%	10.8%
Deep sort	218	6.95x	75.3%	24.4%	35.0%	37.8%

Table 9: Order dependency of binning of 1024×1024 randomly positioned particles in a $128 \times 128 \times 128$ grid.

ordering. Index sorting is not affecting it.

Again differences similarly to the binning can be seen when already working with a sorted state. Coalescing highly increases VRAM throughput. So much that a deep sort on eight `vec4`s is almost on equal footing with a random index sort. The speedup from an uncoalesced to a fully coalesced state is 5.68x. The full sort suffers for each (particle) variable from an uncoalesced access. However if sorting is not done the MPM-Transfers will then suffer from those.

Best Case	$\Delta t_c(\mu s)$	VRAM	Top Stall Reas.	Read	Write
Index	1,516	25.6%	L. Scoreb.(78.7%)	16.30%	9.30%
Full(8 vec4)	1,731	75.3%	L. Scoreb.(92.2%)	38.60%	34.60%
Worst Case	$\Delta t_c(\mu s)$	VRAM	Top Stall Reas.	Read	Write
Index	1,516	26.0%	L. Scoreb.(73.5%)	16.10%	9.40%
Full(8 vec4)	9,847	24.0%	L. Scoreb.(82.2%)	9.90%	14.0%

Table 10: Order dependency of reordering of 1024×1024 randomly positioned particles in a $128 \times 128 \times 128$ grid. Best case is already sorted, worst case is unsorted and still fully random.

Binning as well as reordering will rarely run fully sorted as mentioned in 5.3. Sorting works on the last sorted state. The CFL condition encourages limited reach. Most physical processes will move uniformly. These two properties in general will guarantee higher coalescing as well as L2-cache hit rates. It is however up to the dynamics of the problem how much time is spend sorting.

The following metrics are gathered for PIC-Transfers of momentum as they form a reduced problem to based on only one `vec4` transfer. The MPM-Operations are evaluated with two easily reproducible examples.

For the **G2P-transfers** the different datasets can be seen in table 11 and 12. The first one uses random particle positions and therefore is overly pessimistic for the material point method. Random particle positions as well as random velocities are a configuration that in practice will never occur. Even for a fundamental state of matter of gas this is unrealistic. The second one is optimistic as warp branch divergence is minimized.

The global G2P-transfers does not reach desirable throughput in any of the GPU subunits. The top warp-stall reason is Long Scoreboard: Nearly all information needs to be reloaded uncoalesced from global memory. The data in 12 has an

ordering that encourages data reuse. But is not aligned with the grid. However, the SM already runs on three times its throughput compared to the random data.

Method	$\Delta t_c (\mu s)$	Speedup	L2	SM	Top Warp-Stall Reas.
G2P-global	38,318	-	34.4%	9.6%	L. Scoreb.(95.1%)
sorted	2,991	12.81x	52.3%	67.1%	No Instr.(14.8%)
G2P-shared	9,665	3.96x	2.5%	65.0%	No Instr.(14.2%)

Table 11: G2P-transfers of a $128 \times 128 \times 128$ grid back to one million randomly positioned particles with random velocities between $v_x, v_y, v_z \in [-1.0; 1.0]$. Block size is (8,4,4).

As elucidated in chapter 5.3 deep sorting increases coalescing and caching behavior. The effects of sorting impact performance by a 12.81x speedup in the randomized case. The density of particles per bin is 0.5. Heavy use is made of the L2-Cache rising up to 52.3% reading from many distinctive, successive memory positions. Meanwhile the density of four particles per bin in table 12 puts comparably low strain on the L2-Cache with 9.4%. The runtime on random data is only 12.2% slower than the uniform data.

The G2P-shared method lies miles beyond that as its execution time is 9,665 μs . It can however get an edge on the more favored uniform data where 2,232 is the best recorded time. The G2P-shared method relies on shared memory instead of the L2-Cache to read data. Thus this method can be faster when little branch divergence between warps is the case. The random data however has highly divergent branching and is cause for the high execution times.

Method	$\Delta t_c (\mu s)$	Speedup	L2	SM	Top Warp-Stall Reas.
G2P-global	10,316	-	34.4%	32.4%	L. Scoreb.(79.9%)
sorted	2,629	3.92x	9.4%	66.9%	No Instr.(14.1%)
G2P-shared	2,232	4.62x	4.1%	63.6%	No Instr.(22.7%)

Table 12: G2P-transfers of a $128 \times 128 \times 128$ grid back to one million uniformly positioned particles with random velocities between $v_x, v_y, v_z \in [-1.0; 1.0]$. They form a rotated (unsorted) cube with four particles per cell. Block size is (8,4,4).

In NVIDIA-Nsight run times recorded for the G2P-transfers were comparably lower while making use of batching. However, OpenGL timer queries recorded little difference in trade-off for the added register pressure. Thus G2P-transfers should stay away of batching.

For the sorted G2P-global as well as the G2P-shared method following statements are also of interest. The top-warp stall reason is waiting on the instruction fetches which is typical for compute-bound shaders with high SM usage. The SM Issue Utilization per Active Cycles is consistent around 65%. This indicates that neither increasing occupancy nor reducing warp-stalls would increase performance.

As a summary, relying on the comparably fast L2-Cache memory transactions over shared memory is consistent across the reduced examples for the sorted G2P-global method. The main benefit of the global solution is that warps do not suffer from branch divergence in that method. However, the G2P-shared method may still give an edge in performance.

The **P2G-transfer** is tested on the same data in 13 and 14, respectively. The global atomic approaches suffer from low throughput across all units. Cause are uncoalesced accesses and low cache utilization.

The top stall reason for all global operations is the short scoreboard. This is caused by the high number of atomic writes which are accumulated in L2-Cache. The sorting brings forth this problem more acutely as L2-Caches throughput rises to the top SOL with 44.0% in the uniform case of table 14. The random data example in table 13 relies even more heavily on the L2-Cache with 65.8 SOL% similarly to what has been seen in the G2P-transfer.

Nevertheless, this already speeds up the random case by a factor of 11.88x as it followed no particular ordering. The sorting makes sure that the incoming data is preprocessed for optimal access.

Method	$\Delta t_c (\mu s)$	Speedup	VRAM	L2	SM
global	254,410	-	17.8%	9.6%	1.7%
[Mey15]	217,997	1.17x	21.7%	3.7%	13.2%
[Mey15] sorted	30,477	8.35x	64.2%	64.2%	22.1%
global sorted	21,413	11.88x	7.2%	65.8%	19.4%
P2G-pull	26,822	9.46x	1.6%	2.3%	35.2%
P2G-atomic*	15,552	16.36x	3.7%	7.1%	65.4%
P2G-sync*	12,801	19.87x	3.6%	7.3%	61.3%

Table 13: P2G-transfers of one million randomly positioned particles with random velocities between $v_x, v_y, v_z \in [-1.0; 1.0]$ in a $128 \times 128 \times 128$ grid. Block size is (8,4,4). Methods marked with a star(*) are executed with batching = 4.

Using the **P2G-pull method** on the random case performs worse than the global method. It can significantly save time however in the uniform case. The P2G-pull-transfer is 4.31 times faster than the global P2G-transfer on the sorted uniform data.

Top SOL% is now the SM but it lacks throughput with 39.4%. Its SM Issue Utilization per active cycle is 40% which is below the desired threshold of 60%. The top warp stall reason is instruction based. So as long as the algorithm does not change no increase can be achieved here. As explained in chapter 5.4.2 the pull method requires high amount of shared memory. The occupancy calculator as well as NVIDIA-Nsight report an occupancy of 16.0. This is $\frac{1}{4}$ -th of the maximum occupancy of the GTX970. This is however already optimized for thread group size.

A closer look is taken of the P2G-atomic- and P2G-sync-transfers to illustrate

Method	$\Delta t_c (\mu s)$	Speedup	VRAM	L2	SM
global	44,442	-	4.6 %	34.4%	7.7%
[Mey15]	45,342	0.98x	25.1%	42.4%	11.7%
[Mey15] sorted	23,007	1.97x	43.8%	59.0%	23.9%
global sorted	20,484	2.21x	7.0 %	44.0%	16.1%
P2G-pull	4,747	9.55x	3.7%	6.7%	39.4%
P2G-atomic*	3,148	14.40x	5.3%	6.7%	65.0%
P2G-sync*	2,595	17.47x	5.9%	7.6%	67.0%

Table 14: P2G-transfers of one million uniformly positioned particles with random velocities between $v_x, v_y, v_z \in [-1.0; 1.0]$ in a $128 \times 128 \times 128$ grid. They form a rotated (unsorted) cube with four particles per cell. Block size is (8,4,4). Methods marked with a star(*) are executed with batching = 4.

the performance improvements of batching and filtering for active blocks in table 15.

The **P2G-atomic-Transfer** in its initial state uses one atomic transfer per particle on shared memory. Its effects are quite visible on the SM SOL% with 82.9% to 90.9% in the call for active blocks. The top stall reason is Short Scoreboard which is indicative of the high number of stalls due to atomic writes on shared memory.

Batching reduces the atomic writes. Particles get handled together. In succession one atomic write is done. This changes the top stall reason to the more favorable instruction fetches as the main stall reason with 20.8%. Short scoreboard goes down to 11.6%. As previously the SM was strained, throughput goes down to 65.0%. The greatest time improvement can be seen when batching and indirect call lead to a combined speedup of 2.2x. This is much higher than the multiplicative speedup of 1.51x one could expect.

Method	$\Delta t_c (\mu s)$	Speedup	SM	Top Stall Reas.	Occup.
P2G-atomic	6,933	-	82.9%	S. Scoreb.(24.7%)	43.3
indirect	6,276	1.10x	90.8%	S. Scoreb.(31.7%)	43.4
batching=4	4,929	1.41x	65.1%	No Instr.(20.8%)	34.9
both	3,148	2.20x	65.0%	No Instr.(23.2%)	35.4
P2G-sync	3,161	-	72.4%	No Instr.(17.7%)	43.3
batching=4	2,595	1.21x	67.0%	No Instr.(23.7%)	35.4

Table 15: P2G-transfers of one million uniformly positioned particles with random velocities between $v_x, v_y, v_z \in [-1.0; 1.0]$ in a $128 \times 128 \times 128$ grid. They form a rotated (unsorted) cube with four particles per cell. Block size is (8,4,4). Shown are the effects of filtering active blocks(indirect) and batching.

The **P2G-sync-transfer** also may use batching and save time. The speedups are much smaller with 1.21x in the uniform case of table 15. Batching in this case reduces the amount of thread group barriers needed for synchronization. The warp-

stall reason barrier goes down from 10.4% to 5.8% in this process. The external synchronization is however much less invasive than atomic writes. The P2G-sync method without batching has roughly the same timing as the P2G-atomic-Transfer with batching of four particles.

Batching is a process that adds register pressure as can be seen by the reduced occupancy of 34.9-35.4. Using batching every new particle variable involved in the transfer takes the batching amount of that variables size more registers.

The P2G-atomic-Transfer is very reliant on batching where the P2G-sync-transfer is not. This is further highlighted in table 16. With one particle per cell(area 47.6%) batching does not help at all. The P2G-sync-transfer however can still work comparably fast to either the high density of four particles per cell losing about 7.2% speed or atomic operations because batching is not available. This also means that the P2G-sync-transfer only scales slightly with the area covered which is due to the overhead of loading and writing more blocks.

Method	Area=47.6%	Area=23.8%	Area=11.9%
P2G-sync	3,375 μs	3,266 μs	3,129 μs
batching = 2	-	2,942 μs	2,745 μs
batching = 4	-	-	2,622 μs

Table 16: P2G-sync-transfer of one million uniformly positioned particles with random velocities between $v_x, v_y, v_z \in [-1.0; 1.0]$ in a $128 \times 128 \times 128$ grid. They form a rotated (unsorted) cube with one/two/four particles per cell corresponding to the area of the grid that is covered with 47.6%/23.8%/11.9%. Block size is (4,4,4).

To underline the extensibility of all shaders table 17 implements the APIC-Transfers of chapter 4.5.3. The G2P-shared algorithm continues to lose ground on the global sorted G2P method as its execution time now only measures 300 μs instead of the 400 μs in table 12. Its SM throughput also overtakes the global method with 81.8%.

Method	$\Delta t_c(\mu s)$	SM	Top Stall Reas.	Occup.
G2P(sorted)	3,647	74.9%	No Instr.(14.2%)	57.7
G2P-shared	3,384	81.8%	No Instr.(18.7%)	43.3
P2G-sync	3,843	68.9%	No Instr.(24.9%)	43.3
batching=2	3,634	67.3%	No Instr.(26.5%)	31.6

Table 17: APIC-Transfers of one million uniformly positioned particles with random velocities between $v_x, v_y, v_z \in [-1.0; 1.0]$ in a $128 \times 128 \times 128$ grid. They form a rotated (unsorted) cube with four particles per cell. Block size is (8,4,4). Shown are the effects of filtering active blocks(indirect) and batching.

The P2G-atomic- and the even more favorable P2G-sync-transfer give great speedups over the global atomic methods. Even in a random case (table 13) they

can outdo the global sorted method despite the high branch divergence. They however shine in the uniform case where speedups of 6.5x and 7.8x respectively can be achieved over the global sorted method.

7 Conclusion & Future Work

The derivation of the material point method for a classic elastic material with an implicit midpoint scheme and the APIC scheme ensures that a wide coverage of the method is shown. Although the MPM consists of many mathematical tasks four operations on the GPU can be identified. Exclusive grid and particle operations are parallelized with a 1:1 correspondence to threads. The optional use of stream compaction reduces applicable particles/nodes where necessary.

The other two operations are particle and grid transfers which are the main focus of this thesis. Different particle and grid transfers utilizing the hierarchical memory structure of the GPU are compared. Presented is a pipeline to efficiently execute these transfers on the GPU. All transfers do not rely on fixed bin sizes in any stages of the pipeline. Since these operations are executed multiple times per physical time step these operations are augmented with two preprocessing steps. The preprocessing steps need to be done once and are outweighed by the transfers.

Deep sorting particles with counting sort in a double-buffered manner allows coalesced accesses and high cache hit rates on transfers. Although possible, this process does not rely on the CFL condition. The sorting further guarantees the independence of the ordering of the incoming data and may long-term benefit other operations relying on neighborhood information.

The second preprocessing step is filtering the active blocks of grid and particle transfers with a stream compaction pipeline where no particles are present. It also supplies the P2G-pull- and P2G-sync-transfer with a maximum per block bin counter.

While the shared memory architecture can give an edge in performance it produces branch divergence and may perform worse over a simpler algorithm relying on the L2-cache. The P2G-sync-transfer is shown to be an easily extendable and even in edge cases well performing operation. Particle push transfers could be shown to profit from batching as multiple particles are handled in unison. The sorted global G2P-transfer's consistency of utilizing the L2-Cache is a surprise further to be monitored.

To show the weaknesses and strengths of the transfers tests on an overly pessimistic and an optimistic case are performed and examined. While this strongly furthers understanding it leaves real simulation performance comparisons to be desired.

However, before this process can be concluded merge and split techniques need to be taken into consideration. They are designed to augment the numerics of the material point method but will inherently reduce branch divergence as particle numbers even out between cells in the same warp. As such they will stray less from the optimistic example. The extent to which they will stray from it depends however on the dynamics of the problem.

At the end of this thesis awareness was raised to the following publication [Gao+18] which was simultaneously being worked on. Their decision making is very much alike:

Counting/Histogram sort is also their sorting algorithm of choice in the fashion of [Hoe14]. Instead of reordering any variable, they choose per variable if an index or deep sort is required. Their binning also floors in the same fashion.

The domain decomposition consists of $4 \times 4 \times 4$ blocks, also one of the best options employed here. Instead of filtering the active blocks in the pipeline, they motivate this process earlier by employing a sparse grid structure with fast neighbor queries altogether.

Implemented is a quadratic interpolation instead of a cubic one. The domain shift thus becomes $\frac{h}{2}$ instead of h . Accounting for the larger cubic weighting support, uniform distribution works as fast as the one shown here.

Their main difference in computation is the use of the aforementioned NVIDIA exclusive shuffle operations in the fashion of [Wes15]. These operations largely solve two of the main problems the transfers have.

Instead of needing to rely on shared memory for inter-thread communication, the shuffle operation may be used. Each particle is assigned to a single thread. If for instance the particle size within the $4 \times 4 \times 4$ block exceeds the thread group size, another virtual block may be assigned to the same geometric block.

Each particle in a particle-to-grid-transfer then scatters their contribution to the neighboring grid nodes in a particle push fashion. The transfers are then solved due to segmented parallel reduction where the segments are the variable particle bin sizes. In shared memory this would cause numerous bank conflicts in both the scattering as well as the segmented parallel reduction as elucidated with the block scan of chapter 5.2. The scatter write would also need to be atomic.

This implementation tried to avoid these steps and schedule over grid nodes. This however is the cause of thread divergence which slows down computation for varying bin sizes. Therefore, [Gao+18] will achieve more throughput and better performance in these cases in exchange for a (at the moment) hardware vendor exclusive operation.

Appendices

A D_p for Cubic Splines

```
import numpy as np
from sympy import *

def round_expr(expr, num_digits):
    return expr.xreplace(
        {n : round(n, num_digits) for n in expr.atoms(Number)}
    )

# Limit a,b,c,x to interval [0,1] for simplyfing
a, b, c = symbols('a b c', nonnegative=True)
a = a/(1+a)
b = b/(1+b)
c = c/(1+c)

x = symbols('x', nonnegative=True)
x = x/(1+x)

# Define cubic interpolation function
def N1(x):
    return 0.5*pow(abs(x), 3)-pow(x, 2)+2/3
def N2(x):
    return -1/6*pow(abs(x), 3)+pow(x, 2)-2*abs(x)+4/3
def wip(i, x):
    if(i==1 or i==2):
        return N1(x)
    else:
        return N2(x)

# Define the parametrized position in the grid
def grid_points(x):
    return np.array([-x-1, -x, 1-x, 2-x])

alphas = grid_points(a)
betas = grid_points(b)
gammas = grid_points(c)

D_temp = np.array([[0, 0, 0], [0, 0, 0], [0, 0, 0]])

# Loop over all grid nodes in the vicinity
```

```

for i,ai in enumerate(alphas):
    for j,bj in enumerate(betas):
        for k,ck in enumerate(gammas):
            # xi_xp is the distance from parametrized
            # position to grid node [i,j,k]
            xi_xp = np.array([ai,bj,ck])
            # each outer product weighted by interpolation
            # functions
            this_outer = wip(i,ai)*wip(j,bj)*wip(k,ck)*
                np.outer(xi_xp,xi_xp)
            # summed up over all grid nodes
            D_temp = np.add(D_temp,this_outer)

D = np.array([[0.0,0.0,0.0],
              [0.0,0.0,0.0],
              [0.0,0.0,0.0]])

for i,D_row in enumerate(D_temp):
    for j,D_ij in enumerate(D_row):
        # simplify to cancel polynoms
        # round_expr because of numerical cancellation
        D[i][j] = round_expr(simplify(D_ij),14)
    print(D)

```

Prints out:

$$\begin{bmatrix} 0.33333333 & 0. & 0. \\ 0. & 0.33333333 & 0. \\ 0. & 0. & 0.33333333 \end{bmatrix} = \frac{D_p}{h^2}$$

B Block Scan

Block Scan: Assume a global scan is already computed on a n-dimensional uniform grid. A local scan of an n-dimensional tile/block in that grid can be computed based on this global scan. This again forms a uniform grid. For simplicity assume two dimensions:

Given the initial two-dimensional pre-scan array:

$$\mathbf{G} = \begin{bmatrix} a_{00} & a_{01} & \dots & a_{0n} \\ a_{10} & a_{11} & \dots & a_{1n} \\ \dots & \dots & \dots & \dots \\ a_{m0} & a_{m1} & \dots & a_{mn} \end{bmatrix}. \quad (147)$$

We can identify a block with $i, j, k, l \geq 0, i + k < m$ and $j + l < n$ as:

$$\mathbf{L} = \begin{bmatrix} a_{ij} & a_{(i)(j+1)} & \cdots & a_{(i)(n-l)} \\ a_{(i+1)(j)} & a_{(i+1)(j+1)} & \cdots & a_{(i+1)(n-l)} \\ \cdots & \cdots & \cdots & \cdots \\ a_{(m-k)(j)} & a_{(m-k)(j+1)} & \cdots & a_{(m-k)(n-l)} \end{bmatrix}. \quad (148)$$

We use the Σ -Notation for sums although any associative binary operator would hold. The global scan is computed as all previous rows + the current row to the current element:

$$S_{st}^G = \sum_{q,r=0}^{s-1,n} a_{qr} + \sum_{r=0}^{(t-1)} a_{sr} \quad (149)$$

with $0 \leq s, t \leq m, n$. The local scan is computed similar:

$$S_{bc}^L = \sum_{q,r=i,j}^{(b-1),(n-l)} a_{qr} + \sum_{r=j}^{(c-1)} a_{br}. \quad (150)$$

This however requires a full scan of \mathbf{S}^L , where $i, j \leq b, c \leq (m - k), (n - l)$. We can alternatively compute the local scan from the global scan with the following five steps:

1. Subtract the global scan's first element of every row-element and limit your view to indices b, c then:

$$\begin{aligned} P_{st} &= S_{st}^G - \left(\sum_{q,r=0}^{s-1,n} a_{qr} + \sum_{r=0}^{(j-1)} a_{sr} \right) \\ \Rightarrow P_{bc} &= \sum_{r=j}^{(c-1)} a_{br} \end{aligned} \quad (151)$$

2. Add the last value of \mathbf{L} of the previous row (if it exists) to the current row.

$$\Rightarrow T_{bc} = a_{(b-1)(n-l)} + \sum_{r=j}^{(c-1)} a_{br} \quad (152)$$

3. Extract the last column $c = (n - l)$:

$$t_b = a_{(b-1)(n-l)} + \sum_{r=j}^{(n-l-1)} a_{br}. \quad (153)$$

4. Compute the in dimensionality-by-one reduced exclusive scan (of the last column):

$$s_b = \sum_{q=i}^{(b-1)} \left(a_{(q-1)(n-l)} + \sum_{r=j}^{(n-l-1)} a_{qr} \right). \quad (154)$$

5. Row-wise add back:

$$\begin{aligned} T_{bc} + s_b &= \sum_{q=i}^{(b-1)} \left(a_{(q)(n-l)} + \sum_{r=j}^{(n-l-1)} a_{qr} \right) + \sum_{r=j}^{(c-1)} a_{br} \\ &= \sum_{q=i}^{(b-1)} \sum_{r=j}^{(n-l)} a_{qr} + \sum_{r=j}^{(c-1)} a_{br} = S_{bc}^L. \end{aligned} \quad (155)$$

For a simpler understanding of this process Figure 10 shows the process with the same numbering:

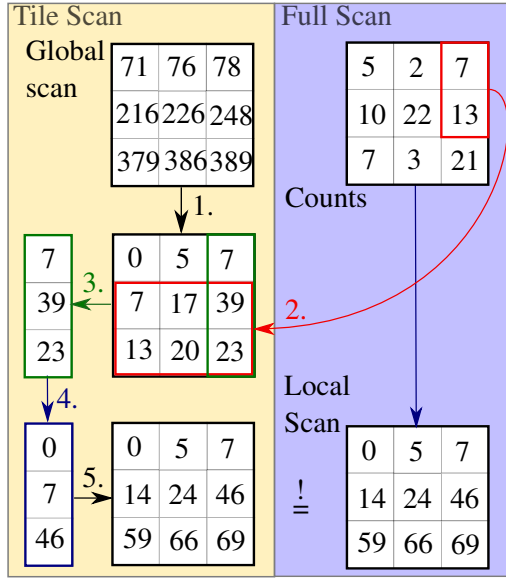


Figure 10: A per block scan following the above enumeration.

C Shared memory accesses on MPM-Transfers

BlockAndHalo(vec4)	0	1	2	3	4	5	6
Banks (1.)	0	1	2	3	4	5	6
Banks (2.)	7	0	1	2	3	4	5
Banks (3.)	6	7	0	1	2	3	4
Banks (4.)	5	6	7	0	1	2	3
Banks (5.)	4	5	6	7	0	1	2
Banks (6.)	3	4	5	6	7	0	1
Banks (7.)	2	3	4	5	6	7	0
Banks (8.)	1	2	3	4	5	6	7
Banks (9.)	0	1	2	3	4	5	6

Table 18: First run of transfer: Bank accesses by warp with block size $x = 4$. Bank accesses are colored grey. The halo ranges due to the support from 0 – 7. Every bank gets accessed four times. It is easy to see that a window shift would lead to the same amount of bank accesses.

BlockAndHalo(vec4)	0	1	2	3	4	5	6	7	8	9	10
Banks (1.)	0	1	2	3	4	5	6	7	0	1	2
Banks (2.)	3	4	5	6	7	0	1	2	3	4	5
Banks (3.)	6	7	0	1	2	3	4	5	6	7	0
Banks (4.)	1	2	3	4	5	6	7	0	1	2	3
Banks (5.)	4	5	6	7	0	1	2	3	4	5	6

Table 19: First run of transfer: Bank accesses by warp with block size $x = 8$. Bank accesses are colored grey. The halo ranges due to the support from 0 – 10. Every bank gets accessed four times. It is easy to see that a window shift would lead to the same amount of bank accesses.

List of Figures

1	SoA-Layout in practice. The first instruction is shown in orange, the second instruction in green. If green is left out throughput is still maximized	37
2	AoS-Layout in practice. The first instruction is shown in orange, the second instruction in green. Orange already loads both cache-lines. If green is left out throughput is halved. Also green is an L2-cache lookup requiring additional overhead over the direct SoA way.	37
3	Sequential addressing for <code>vec4s</code> . Even threads are blue. Odd threads are yellow. Shared-memory banks per instruction are colored: The banks of the first instruction are green and red numbers. The second instruction is only green. The first and all following instructions can be handled fully concurrently. No memory padding is required.	38
4	Scan (add)	39
5	Interleaved addressing <code>vec4s</code> . Even threads are blue, odd are yellow. Shared-memory banks per instruction are colored: The banks of the first instruction are green and red numbers. The second instruction is only green. Memory padding needs to be done for concurrent shared-memory access. The first and all following instructions can be handled fully concurrently.	40
6	Binning: Particle adds one to c_i after storing it as o_p	41
7	G2P-transfer: The transfer of a single particle is split into 64 sequential runs (using cubic weights). Shown are the first two runs.	45
8	P2G-transfer: The first run is shown. On the left the P2G-sync-transfer is shown that writes into the neighborhood. On the right the P2G-pull approach is shown that instead reads out of the neighborhood.	47
9	Pipeline to filter active blocks. Returned is the number of active blocks for the launch of a dispatch. A scan and an indexed stream compaction give back the filtered indices to access the active blocks in that dispatch.	49
10	A per block scan following the above enumeration.	67

List of Tables

1	GPU Memory [NVib]	32
2	GPU Performance Metrics	35
3	Error of various shaders on 1024*1024 random elements. Scalars are just between [0.0-1.0]. The vectors have a length between [0.0-1.0].	51

4	Error of 1,000 PIC/APIC-roundtrips of 1M uniformly placed particles with random velocity in a $128 \times 128 \times 128$ grid. Used this instance is a P2G-sync-transfer and G2P-transfer with batching = 4 and block size = (4,4,4). Particles are fixed.	52
5	Metrics between different buffer layouts. Map operation with one instruction <code>float x = length(vel)</code> on 1024×1024 <code>vec4</code> buffer storing position and velocity (<code>vel</code>).	53
6	Metrics between different buffer layouts. Map operation with two instructions <code>float x = length(vel), float y = length(pos)</code> on 1024×1024 <code>vec4</code> buffer storing position(<code>pos</code>) and velocity (<code>vel</code>).	53
7	Optimization of one parallel reduction dispatch on 1024×1024 <code>vec4</code> with <code>unary_op(vec4 x)=length(x)</code> with <code>block_size = 1024</code> . Δt_c is in μs . Note that, the interleaved addressing in this example intentionally commits bank conflicts to show performance impacts. The number in parentheses states the number of additional added sequential elements. Reduced is by <code>block_size</code> \times sequential elements. Thus they do more work, while also performing better!	54
8	Optimization of one scan dispatch on $4 \times 1024 \times 1024$ integers with <code>binary_op(x, y) := x+y</code> . Δt_c in μs , block size is 1024. The number in parentheses states the number of additionally loaded sequential elements. Segment of each scan is <code>block_size</code> \times sequential elements. Higher reduction factor corresponds to more work being done.	55
9	Order dependency of binning of 1024×1024 randomly positioned particles in a $128 \times 128 \times 128$ grid.	56
10	Order dependency of reordering of 1024×1024 randomly positioned particles in a $128 \times 128 \times 128$ grid. Best case is already sorted, worst case is unsorted and still fully random.	56
11	G2P-transfers of a $128 \times 128 \times 128$ grid back to one million randomly positioned particles with random velocities between $v_x, v_y, v_z \in [-1.0; 1.0]$. Block size is (8,4,4).	57
12	G2P-transfers of a $128 \times 128 \times 128$ grid back to one million uniformly positioned particles with random velocities between $v_x, v_y, v_z \in [-1.0; 1.0]$. They form a rotated (unsorted) cube with four particles per cell. Block size is (8,4,4).	57
13	P2G-transfers of one million randomly positioned particles with random velocities between $v_x, v_y, v_z \in [-1.0; 1.0]$ in a $128 \times 128 \times 128$ grid. Block size is (8,4,4). Methods marked with a star(*) are executed with batching = 4.	58

14	P2G-transfers of one million uniformly positioned particles with random velocities between $v_x, v_y, v_z \in [-1.0; 1.0]$ in a $128 \times 128 \times 128$ grid. They form a rotated (unsorted) cube with four particles per cell. Block size is (8,4,4). Methods marked with a star(*) are executed with batching = 4.	59
15	P2G-transfers of one million uniformly positioned particles with random velocities between $v_x, v_y, v_z \in [-1.0; 1.0]$ in a $128 \times 128 \times 128$ grid. They form a rotated (unsorted) cube with four particles per cell. Block size is (8,4,4). Shown are the effects of filtering active blocks(indirect) and batching.	59
16	P2G-sync-transfer of one million uniformly positioned particles with random velocities between $v_x, v_y, v_z \in [-1.0; 1.0]$ in a $128 \times 128 \times 128$ grid. They form a rotated (unsorted) cube with one/two/four particles per cell corresponding to the area of the grid that is covered with 47.6%/23.8%/11.9%. Block size is (4,4,4).	60
17	APIC-Transfers of one million uniformly positioned particles with random velocities between $v_x, v_y, v_z \in [-1.0; 1.0]$ in a $128 \times 128 \times 128$ grid. They form a rotated (unsorted) cube with four particles per cell. Block size is (8,4,4). Shown are the effects of filtering active blocks(indirect) and batching.	60
18	First run of transfer: Bank accesses by warp with block size $x = 4$. Bank accesses are colored grey. The halo ranges due to the support from 0 – 7. Every bank gets accessed four times. It is easy to see that a window shift would lead to the same amount of bank accesses.	68
19	First run of transfer: Bank accesses by warp with block size $x = 8$. Bank accesses are colored grey. The halo ranges due to the support from 0 – 10. Every bank gets accessed four times. It is easy to see that a window shift would lead to the same amount of bank accesses.	68

Algorithms and source code

1	Conjugate gradient	30
2	AoS-Layout	36
3	SoA-Layout	36
4	OpenGL Layout	36
5	G2P-transfer	46
6	P2G-sync-transfer	48

References

- [Aal] Sebastian Aaltonen. *Optimizing GPU occupancy and resource usage with large thread groups*. <https://gpuopen.com/optimizing-gpu-occupancy-resource-usage-large-thread-groups/>. [Online; accessed 26-September-2018].
- [Abe12] Rohan Abeyaratne. *Volume II of Lecture Notes on, The Mechanics of Elastic Solids: Continuum Mechanics*. http://web.mit.edu/abeyaratne/Volumes/RCA_Vol_II.pdf. [Online; accessed 08-November-2018]. MIT Department of Mechanical Engineering, 2012.
- [AER] MIT AEROASTRO. *16.20 Structural Mechanics, Module Notes 3: Constitutive Equations*. http://web.mit.edu/16.20/homepage/3_Constitutive/Constitutive_files/module_3_no_solutions.pdf. [Online; accessed 07-November-2018]. Massachusetts Institute of Technology, Department of Aeronautics and Astronautics.
- [Bat06] Klaus-Jürgen Bathe. *Finite element procedures*. Klaus-Jurgen Bathe, 2006.
- [Bav] Louis Bavoil. *The Peak-Performance Analysis Method for Optimizing Any GPU Workload*. <https://devblogs.nvidia.com/the-peak-performance-analysis-method-for-optimizing-any-gpu-workload>. [Online; accessed 15-September-2018]. NVIDIA Corporation.
- [Bax13] Sean Baxter. *Reduce and Scan*. <https://moderngpu.github.io/scan.html>. [Online; accessed 15-October-2018]. NVIDIA Corporation, 2013.
- [BP10] Tobias Brandvik and Graham Pullan. “SBLOCK: A framework for efficient stencil-based PDE solvers on multi-core platforms”. In: *2010 IEEE 10th International Conference on Computer and Information Technology (CIT)*. IEEE. 2010, pp. 1181–1188.
- [Bur+10] Heiko Burau et al. “PConGPU: a fully relativistic particle-in-cell code for a GPU cluster”. In: *IEEE Transactions on Plasma Science* 38.10 (2010), pp. 2831–2839.
- [Cra+11] Cyril Crassin et al. “Interactive indirect illumination using voxel cone tracing”. In: *Computer Graphics Forum*. Vol. 30. 7. Wiley Online Library. 2011, pp. 1921–1930.
- [DR08] W. Dahmen and A. Reusken. *Numerik für Ingenieure und Naturwissenschaftler*. Springer-Lehrbuch. Springer Berlin Heidelberg, 2008. ISBN: 9783540764939.
- [DS11] Viktor K Decyk and Tajendra V Singh. “Adaptable particle-in-cell algorithms for graphical processing units”. In: *Computer Physics Communications* 182.3 (2011), pp. 641–648.

- [EHB57] Martha W Evans, Francis H Harlow, and Eleazer Bromberg. *The particle-in-cell method for hydrodynamic calculations*. Tech. rep. LOS ALAMOS NATIONAL LAB NM, 1957.
- [Fre] Free Software Foundation, Inc. *The C Preprocessor*. <https://gcc.gnu.org/onlinedocs/cpp>. [Online; accessed 28-January-2019].
- [Fu+17] Chuyuan Fu et al. “A polynomial particle-in-cell method”. In: *ACM Transactions on Graphics (TOG)* 36.6 (2017), p. 222.
- [Gao+17] Ming Gao et al. “An adaptive generalized interpolation material point method for simulating elastoplastic materials”. In: *ACM Transactions on Graphics (TOG)* 36.6 (2017), p. 223.
- [Gao+18] Ming Gao et al. “GPU Optimization of Material Point Methods”. In: *ACM Trans. Graph.* 37.6 (2018), 254:1–254:12. ISSN: 0730-0301.
- [Gas+15] Theodore F Gast et al. “Optimization integrator for large time steps”. In: *IEEE transactions on visualization and computer graphics* 21.10 (2015), pp. 1103–1115.
- [GM77] Robert A Gingold and Joseph J Monaghan. “Smoothed particle hydrodynamics: theory and application to non-spherical stars”. In: *Monthly notices of the royal astronomical society* 181.3 (1977), pp. 375–389.
- [Gon00] Oscar Gonzalez. “Exact energy and momentum conserving algorithms for general models in nonlinear elasticity”. In: *Computer Methods in Applied Mechanics and Engineering* 190.13-14 (2000), pp. 1763–1783.
- [Guo+18] Qi Guo et al. “A Material Point Method for Thin Shells with Frictional Contact”. In: *ACM Trans. Graph.* 37.4 (July 2018), pp. 147.1–147.15.
- [Har07] Mark Harris. “Optimizing parallel reduction in CUDA”. In: *Proc. ACM SIGMOD* 21 (Jan. 2007), pp. 104–110.
- [Hoe14] Rama Hoetzlein. *Fast Fixed-Radius Nearest Neighbors: Interactive Million-Particle Fluids*. <http://on-demand.gputechconf.com/gtc/2014/presentations/S4117-fast-fixed-radius-nearest-neighbor-gpu.pdf>. [Online; accessed 30-September-2018]. NVIDIA Corporation, 2014.
- [Hön+] Wolfgang Hönig et al. “A generic approach for developing highly scalable particle-mesh codes for gpus”. In:
- [HSO07] Mark Harris, Shubhabrata Sengupta, and John D Owens. “Parallel prefix sum (scan) with CUDA”. In: *GPU gems* 3.39 (2007), pp. 851–876.
- [JG13] Benoît Jacob and Gaël Guennebaud. *Eigen: A C++ linear algebra library*. [Online; accessed 19-January-2019]. 2013.

- [Jia+15] Chenfanfu Jiang et al. “The affine particle-in-cell method”. In: *ACM Transactions on Graphics (TOG)* 34.4 (2015), p. 51.
- [Jia+16] Chenfanfu Jiang et al. “The material point method for simulating continuum materials”. In: *ACM SIGGRAPH 2016 Courses*. ACM. 2016, p. 24.
- [JST17] Chenfanfu Jiang, Craig Schroeder, and Joseph Teran. “An angular momentum conserving affine-particle-in-cell method”. In: *Journal of Computational Physics* 338 (2017), pp. 137–164.
- [KD13] Marcin Krotkiewski and Marcin Dabrowski. “Efficient 3D stencil computations using CUDA”. In: *Parallel Computing* 39.10 (2013), pp. 533–548.
- [Khr12] Khronos Group. *OpenGL Wiki: Compute Shader, Shared memory coherency*. [Online; accessed 16-January-2019]. 2012.
- [Klá+16] Gergely Klár et al. “Drucker-prager elastoplasticity for sand animation”. In: *ACM Transactions on Graphics (TOG)* 35.4 (2016), p. 103.
- [Klá+17] Gergely Klár et al. “Production ready MPM simulations”. In: *ACM SIGGRAPH 2017 Talks*. ACM. 2017, p. 42.
- [Kon+11] Xianglong Kong et al. “Particle-in-cell simulations with charge-conserving current deposition on graphic processing units”. In: *Journal of Computational Physics* 230.4 (2011), pp. 1676–1685.
- [McA+11a] Aleka McAdams et al. “Computing the singular value decomposition of 3×3 matrices with minimal branching and elementary floating point operations”. In: *Tech. Rep. 1690 University of Wisconsin-Madison* (2011).
- [McA+11b] Aleka McAdams et al. “Efficient elasticity for character skinning with contact and collisions”. In: *ACM Transactions on Graphics (TOG)* 30.4 (2011), p. 37.
- [McG] Bob McGinty. *Continuum Mechanics*. <http://www.continuummechanics.org/basicmath.html>. [Online; accessed 08-November-2018].
- [Mey15] Fabian Meyer. “Simulation von Schnee”. Bachelor’s Thesis. Universität Koblenz-Landau, Institut für Computervisualistik, 2015.
- [Mic17] Scott Michaud. *OpenCL: Merging Roadmap into Vulkan*. <https://www.pcper.com/reviews/General-Tech/Breaking-OpenCL-Merging-Roadmap-Vulkan>. [Online; accessed 24-January-2019]. 2017.

- [MIT] MITOPENCOURSEWARE. *18.06 Linear Algebra, Unit III. Lecture Summary: Singular value decomposition*. https://ocw.mit.edu/courses/mathematics/18-06sc-linear-algebra-fall-2011/positive-definite-matrices-and-applications/singular-value-decomposition/MIT18_06SCF11_Ses3.5sum.pdf. [Online; accessed 14-November-2018]. MIT Department of Mechanical Engineering.
- [NVIa] NVIDIA Corporation. *Achieved Occupancy*. <https://docs.nvidia.com/gameworks/content/developertools/desktop/analysis/report/cudaexperiments/kernellevel/achievedoccupancy.htm>. [Online; accessed 4-December-2018].
- [NVIb] NVIDIA Corporation. *Best Practices Guide - v10.0.130*. <https://docs.nvidia.com/cuda/cuda-c-best-practices-guide>. [Online; accessed 26-September-2018].
- [NVIc] NVIDIA Corporation. *CUDA Occupancy Calculator*. <https://docs.nvidia.com/cuda/cuda-c-best-practices-guide>. [Online; accessed 3-December-2018].
- [NVId] NVIDIA Corporation. *GeForce GTX 970 Specifications*. <https://www.geforce.com/hardware/desktop-gpus/geforce-gtx-970/specifications>. [Online; accessed 28-January-2019].
- [NVIf] NVIDIA Corporation. *Maxwell Tuning Guide*. <https://docs.nvidia.com/cuda/maxwell-tuning-guide/#l1-cache>. [Online; accessed 5-December-2018].
- [NVIf] NVIDIA Corporation. *NVEmulate*. <https://developer.nvidia.com/nvemulate>. [Online; accessed 3-December-2018].
- [NVIg] NVIDIA Corporation. *NVIDIA Nsight*. https://docs.nvidia.com/nsight-visual-studio-edition/Content/Performance_Markers_OGL.htm. [Online; accessed 5-December-2018].
- [Öch14] Andreas Öchsner. *Elasto-plasticity of frame structure elements, Chapter 2: Continuum Mechanics of Plasticity*. Springer, 2014.
- [Pay12] Joshua Estes Payne. “Implementation and performance evaluation of a GPU particle-in-cell code”. MA thesis. Massachusetts Institute of Technology, 2012.
- [Pie14] Daniell Piers. *GL_ARB_timer_query*. https://www.khronos.org/registry/OpenGL/extensions/ARB/ARB_timer_query.txt. [Online; accessed 15-September-2018]. The Khronos Group Inc., 2014.
- [Pol] Antony Polukhin. *magic_{get}*. https://github.com/apolukhin/magic_get. [Online; accessed 3-December-2018].

- [Ram+15] Daniel Ram et al. “A material point method for viscoelastic fluids, foams and sponges”. In: *Proceedings of the 14th ACM SIGGRAPH/Eurographics Symposium on Computer Animation*. ACM. 2015, pp. 157–163.
- [Ros13] Francesco Rossi. *Particle in cell simulations on GPU clusters*. https://hifweb.lbl.gov/public/BLAST/seminars/2013_05_21/21-05-2013_afrd_Francesco_Rossi.pdf. [Online; accessed 26-September-2018]. 2013.
- [Sch] Tim C. Schroeder. *Memory Bandwidth Limited Kernels*. http://developer.download.nvidia.com/CUDA/training/bandwidthlimitedkernels_webinar.pdf. [Online; accessed 3-December-2018].
- [SDG08] George Stantchev, William Dorland, and Nail Gumerov. “Fast parallel particle-to-grid interpolation for plasma PIC simulations on the GPU”. In: *Journal of Parallel and Distributed Computing* 68.10 (2008), pp. 1339–1349.
- [SKB08] Michael Steffen, Robert M Kirby, and Martin Berzins. “Analysis and reduction of quadrature errors in the material point method (MPM)”. In: *International journal for numerical methods in engineering* 76.6 (2008), pp. 922–948.
- [Sto+12] Alexey Stomakhin et al. “Energetically consistent invertible elasticity”. In: *Proceedings of the 11th ACM SIGGRAPH/Eurographics conference on Computer Animation*. 2012, pp. 25–32.
- [Sto+13] Alexey Stomakhin et al. “A material point method for snow simulation”. In: *ACM Transactions on Graphics (TOG)* 32.4 (2013), p. 102.
- [Sto+14] Alexey Stomakhin et al. “Augmented MPM for phase-change and varied materials”. In: *ACM Transactions on Graphics (TOG)* 33.4 (2014), p. 138.
- [Str07] G. Strang. *Computational Science and Engineering*. Wellesley-Cambridge Press, 2007. ISBN: 9780961408817.
- [Sym] SymPy Development Team. *SymPy: A Python library for symbolic mathematics*. <https://www.sympy.org/en/index.html>. [Online; accessed 20-November-2018].
- [SZS95] Deborah Sulsky, Shi-Jian Zhou, and Howard L Schreyer. “Application of a particle-in-cell method to solid mechanics”. In: *Computer physics communications* 87.1-2 (1995), pp. 236–252.
- [Tam+17] Andre Pradhana Tampubolon et al. “Multi-species simulation of porous sand and water mixtures”. In: *ACM Transactions on Graphics (TOG)* 36.4 (2017), p. 105.

- [Wes15] Elmar Westphal. *Voting and Shuffling to Optimize Atomic Operations*. <https://devblogs.nvidia.com/voting-and-shuffling-optimize-atomic-operations>. [Online; accessed 02-October-2018]. NVIDIA Corporation, 2015.
- [Wil+07] Samuel Williams et al. “Scientific computing kernels on the cell processor”. In: *International Journal of Parallel Programming* 35.3 (2007), pp. 263–298.